國立臺灣大學工學院化學工程學系

碩士論文

Department of Chemical Engineering

College of Engineering

National Taiwan University

Master's Thesis

含鐵有機金屬框架結合具生物相容性之微針系統於局部經皮應用

Biocompatible Microneedle Systems Loaded with Iron-Based Metal-Organic Frameworks for Localized Transdermal Application

翁在萱

Tzay-Shiuan Ueng

指導教授: 吳嘉文 博士

Advisor: Kevin C.-W. Wu, Ph.D.

中華民國 114 年 7 月

July 2025

doi:10.6342/NTU202501655

國立臺灣大學碩士學位論文
口試委員會審定書
MASTER'S THESIS ACCEPTANCE CERTIFICATE
NATIONAL TAIWAN UNIVERSITY

含鐵有機金屬框架結合具生物相容性之微針系統於局部經皮應用

Biocompatible Microneedle Systems Loaded with Iron-Based Metal-Organic Frameworks for Localized Transdermal Application

本論文係 翁在萱(R12524138) 在國立臺灣大學化學工程學系完成之碩士學位論文，於民國 114 年 6 月 30 日承下列考試委員審查通過及口試及格，特此證明。

The undersigned, appointed by the Department / Graduate Institute of Chemical Engineering on 30th June 2025 have examined a Master's Thesis entitled above presented by Tzay-Shiuan Ueng (R12524138) candidate and hereby certify that it is worthy of acceptance.

口試委員 Oral examination committee:

（指導教授 Advisor）

系（所、學位學程）主管 Director:

致謝

2025 年夏季，我完成了這篇論文，在離開校園之前，我想好好感謝這一路上幫助過我的人。

首先，我想感謝我的指導教授，吳嘉文老師，感謝老師一開始願意收考試突然候補上，在迷茫能去往哪間實驗室的我，也謝謝老師這兩年來給予的大量資源與機會，讓我參加各種研討會及展覽並能夠自由地做研究。老師一直很注重邏輯的通順，我想這對未來的我一定也會是非常有幫助的。接著，我想感謝長庚醫院的高煌凱醫師，謝謝您一直以來都願意抽出時間跟我們開會，並也給予建議，也謝謝高醫師的助理—小新及安妮，提供細胞讓我們做實驗，並花時間帶著我們操作。謝謝清大的李亦淇老師，在口試中給予大量建議以及未來可以做的方向，也謝謝李老師實驗室的學生—姿涵學姊以及芷瑜，協助我設計出部分實驗。同時，我也想對莊爾元老師以及陳靖昀老師表達感謝，謝謝您們擔任我的口試委員，並且對我的研究及口試內容給出了肯定以及建議。

感謝實驗室的同學，首先要謝謝博修學長，兩年來給我的研究建議。謝謝祐陞學長，從 0 開始教我做細胞實驗，讓我後來在長庚操作得比較順利。謝謝楚仁學長，教我用很多研究用得到的軟體。感謝顗平給我很多投影片的建議，謝謝陳彥璋及文哲在國衛院作伴，謝謝蔡捷仔分享有趣故事，也謝謝芷欣繼承我的研究。謝謝淑萍學姊幫我處理很多國衛院的行政。感謝廖英志老師實驗室的郭景泰，幫我 3D 列印實驗用的模具。謝謝游佳欣老師實驗室的籃冠宇，幫我處理一些實驗上的事務。還有方致捷在我到新竹的時候擔任地主隊，陪我吃飯。謝謝鍾偉庭一開始引薦我加入 Wu lab。感謝上述所有人的幫助，沒有你們，這篇論文是不可能完成的。

最後，我想謝謝我的家人，給予我經濟上以及情緒上的價值。謝謝泥翊涵巴巴跟我互傳廢片，謝謝黃奕愷，陪我打遊戲也接收我的負面情緒，謝謝你們。

doi:10.6342/NTU202501655

摘要

皮膚纖維化是由於正常的傷口修復機制失調，導致過度膠原蛋白生成並形成異常疤痕。本研究提出一種具生物相容性的經皮藥物傳輸系統，將含鐵之有機金屬框架材料（MIL-100(Fe)）結合於可溶性微針貼片中，並選用聚乙烯醇（PVA）或羧甲基纖維素鈉（CMC）作為基材。MIL-100(Fe)藉由微波輔助水熱法合成，並透過 X 光繞射（XRD）、掃描式電子顯微鏡（SEM）、穿透式電子顯微鏡（TEM）、氮氣吸附脫附測試與動態光散射（DLS）等技術進行結構與物性分析，結果證實其具備良好的結構完整性、形貌均勻性與穩定性。細胞毒性測試顯示，MIL-100(Fe)對人類蟹足腫纖維母細胞在最高至 500 μg/mL 的濃度下仍保有 90%以上的細胞存活率，展現出優異的生物相容性。機械性質分析指出，7 wt%的 CMC 擁有較 7 wt%的 PVA 更高的楊氏模數，但兩者皆需進一步優化以達成理想的皮膚穿透能力。豬皮體外實驗顯示，相較於固定力插入，施加瞬間手部壓力能有效提升微針穿透效果。綜合而言，本研究所開發之 MIL-100(Fe)載藥微針系統具備局部、微創治療皮膚纖維化的潛力，未來可透過微針結構與材料成分的調整進一步優化其治療效果。

關鍵字：皮膚纖維化、微針、經皮藥物輸送、有機金屬框架、MIL-100(Fe)

doi:10.6342/NTU202501655

Abstract

Skin fibrosis arises when normal wound repair becomes dysregulated, leading to excessive collagen production and the formation of abnormal scars. This study proposes a biocompatible transdermal delivery system that incorporates iron-based metal-organic frameworks (i.e., MIL-100(Fe)) into dissolvable microneedle patches made from polyvinyl alcohol (PVA) or sodium carboxymethyl cellulose (CMC). MIL-100(Fe) was synthesized through a microwave-assisted hydrothermal method, and it was characterized using X-ray diffraction (XRD), scanning electron microscopy (SEM), transmission electron microscopy (TEM), N_2 adsorption/desorption, and dynamic light scattering (DLS) analyses. These characterizations confirmed its structure, uniform morphology, and good colloidal stability. Cytotoxicity tests conducted on human keloid fibroblasts indicated high cell viability of over 90% at concentrations up to 500 μg/mL, demonstrating excellent biocompatibility. Mechanical analysis showed that 7 wt% CMC exhibited a higher Young's modulus than 7 wt% PVA. However, both polymers will require further optimization to ensure complete skin penetration. *In vitro* tests on porcine skin revealed that applying microneedles with manual pressure resulted in better insertion compared to a constant-force application. Overall, the MIL-100(Fe)-loaded microneedle system offers a promising strategy for the localized, minimally invasive treatment of skin

doi:10.6342/NTU202501655

fibrosis, with potential for further refinement in both structure and composition.

Keywords: Skin fibrosis, microneedle, transdermal drug delivery, metal-organic frameworks (MOFs), MIL-100(Fe)

doi:10.6342/NTU202501655

Table of Contents

doi:10.6342/NTU202501655

doi:10.6342/NTU202501655

doi:10.6342/NTU202501655

doi:10.6342/NTU202501655

List of Figures

doi:10.6342/NTU202501655

doi:10.6342/NTU202501655

doi:10.6342/NTU202501655

doi:10.6342/NTU202501655

doi:10.6342/NTU202501655

doi:10.6342/NTU202501655

List of Tables

doi:10.6342/NTU202501655

1. Introduction

1.1. Skin fibrosis

1.1.1. Wound healing process

Wound healing is a natural and well-organized process that happens in four main stages, including hemostasis, inflammation, proliferation, and remodeling[1]. Immediately after an injury, blood vessels constrict and platelets aggregate to form a clot, preventing further bleeding. These platelets also release growth factors like transforming growth factor-beta (TGF-β) and platelet-derived growth factor (PDGF), which initiate the healing process[2]. In the inflammatory phase, immune cells such as neutrophils and macrophages move to the wound site to remove debris and pathogens, while also secreting cytokines that promote healing progression[1]. In the proliferative phase, fibroblasts are activated to produce extracellular matrix (ECM) like collagen III and fibronectin, angiogenesis builds new blood vessels, and re-epithelialization allows skin cells to close the wound[3]. Some fibroblasts differentiate into myofibroblasts, enabling wound contraction[4]. In the final remodeling phase, collagen III is gradually replaced by collagen I, and cellular activity declines as the tissue returns to its normal strength and structure[5] (**Fig. 1.1**).

doi:10.6342/NTU202501655

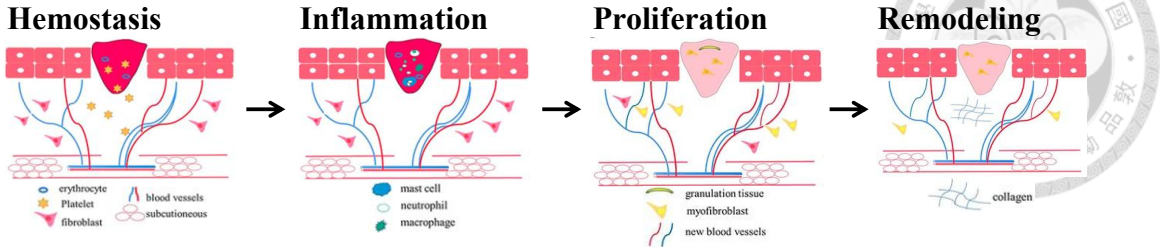

Fig. 1.1. The normal wound healing process[6].

1.1.2. Abnormal scars

Although most skin wounds heal through a well-regulated process, disruptions caused by prolonged inflammation, excessive fibroblast activity, or imbalanced signaling pathways can lead to abnormal wound healing, which may result in excessive scarring, such as hypertrophic scars and keloids[7]. These pathological scars are characterized by the abnormal accumulation of collagen, mainly types I and III, along with persistent myofibroblast activation and a disorganized ECM structure[8]. Hypertrophic scars usually form within weeks after injury, remain within the original wound boundaries, and may regress over time[9]. Keloids, in contrast, often develop months or even years later, grow beyond the wound boundary, and rarely resolve on their own[9] (**Fig. 1.2**). Histologically, hypertrophic scars exhibit parallel collagen alignment and dense vascularization, whereas keloids show irregular collagen bundles, less contraction, and more cellular activity at the periphery[10]. At the molecular level, TGF-β plays a key regulatory role. Elevated

doi:10.6342/NTU202501655

expression of TGF-β1 and TGF-β2 promotes fibrosis through fibroblast activation and collagen production[11]. In contrast, TGF-β3, which normally helps reduce scarring, is often found at lower levels in abnormal scars[11]. Additionally, inflammatory signals like interleukin-6 (IL-6) and IL-8 are also increased, while the anti-inflammatory IL-10 is reduced, further shifting the healing response toward fibrosis[12].

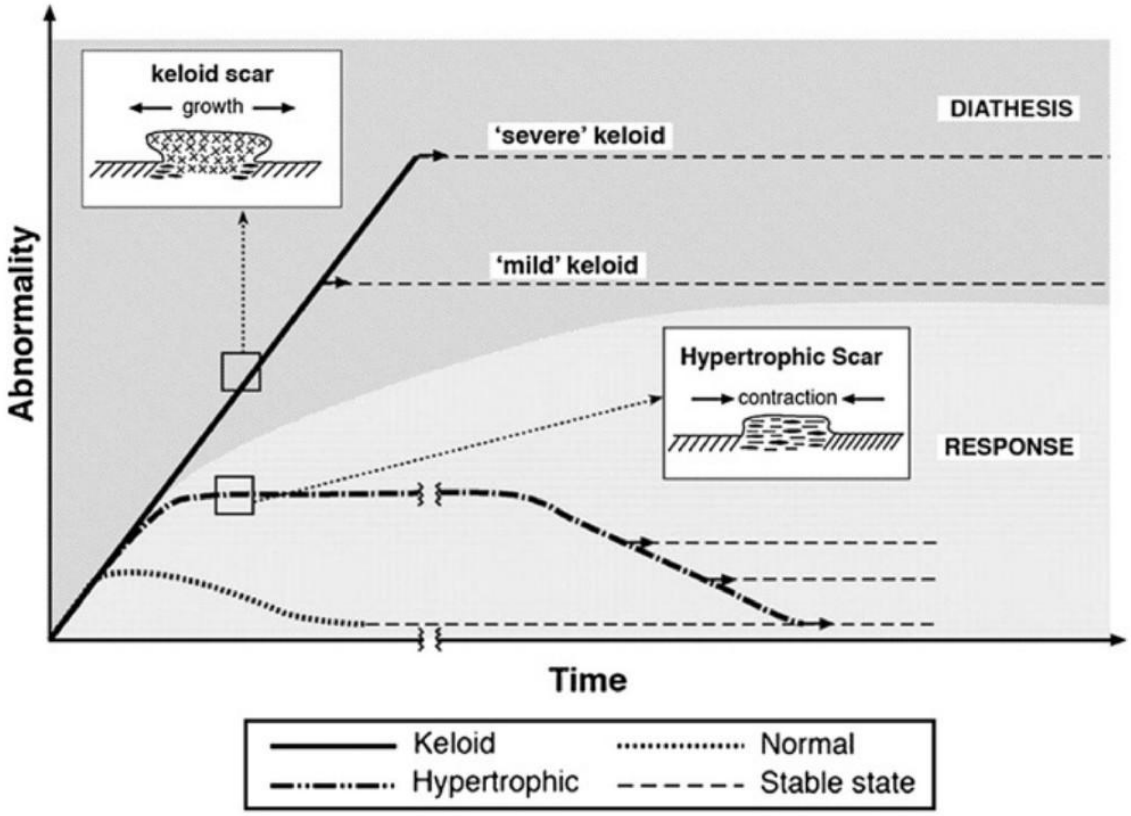

Fig. 1.2. Schematic comparison of scar progression over time in normal healing, hypertrophic scars, and keloid scars[13].

doi:10.6342/NTU202501655

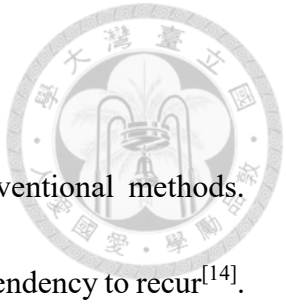

1.1.3. Current treatments

Hypertrophic scars and keloids are treated using various conventional methods. Current treatments often involve multimodal approaches due to their tendency to recur[14]. Silicone gel sheets and compression therapy are commonly used as non-invasive options to flatten scars and improve texture by maintaining hydration and applying mechanical pressure[14]. Intralesional corticosteroids, especially triamcinolone acetonide, are widely applied to suppress inflammation and collagen production[15]. For more severe cases, surgical excision may be performed, often combined with steroid injections or radiation therapy to reduce recurrence[16]. Additional options such as cryotherapy and laser therapy are also used as supplementary treatments, depending on scar characteristics[17].

1.2. Metal-organic frameworks (MOFs) in biomedical applications

Metal-organic frameworks (MOFs) are crystalline porous materials composed of metal clusters and organic ligands. Their exceptional structural tunability, chemical functionality, and internal porosity have made MOFs increasingly appealing in the biomedical field[18]. Among the various types of MOFs, iron-based MOFs such as MIL-100(Fe) have been extensively studied due to their advantageous biological properties, including low toxicity, biodegradability, and modifiable surfaces that support further

doi:10.6342/NTU202501655

functionalization[19]. MIL-100(Fe) consists of iron clusters connected by organic linkers, forming a porous network capable of efficiently encapsulating therapeutic agents and enabling controlled release. This material exhibits good material stability in biological environments and can be synthesized using water-based or solvent-free methods, enhancing its suitability for biomedical applications[20]. Furthermore, its gradual degradation in biological media provides opportunities for sustained drug release while reducing concerns regarding long-term accumulation[20]. In previous studies, MIL-100(Fe) has been investigated primarily as a nanocarrier for anticancer agents, with drug release profiles that are responsive to environmental triggers such as pH and redox potential. Its surface can also be modified with polymers or other nanostructures to improve colloidal stability, cellular uptake, and imaging functionalities[21]. Beyond cancer therapy, MIL-100(Fe) has also shown potential in other biomedical fields, including antimicrobial applications, phototherapy, and biosensing[20]. Given iron's relatively low cytotoxicity, MIL-100(Fe) is considered a safer alternative to many other MOFs for therapeutic use. However, further research is required to optimize its large-scale production, clarify its degradation mechanisms *in vivo*, and assess long-term biocompatibility in clinical applications[20].

Based on previous studies demonstrating that iron chelators such as deferoxamine

doi:10.6342/NTU202501655

(DFO) can enhance wound healing by stabilizing HIF-1α and promoting neovascularization[22], we hypothesized that an iron-based approach may elicit the opposite effect. In addition to existing studies, recent investigations from our group have demonstrated that MIL-100(Fe) significantly reduces the expression of fibrosis-associated markers, including TGF-β and HIF-1α, in keloid fibroblasts. These findings suggest the potential of MIL-100(Fe) in modulating the fibrotic microenvironment. A detailed report of this work is currently under review.

1.3. Transdermal drug delivery

Transdermal drug delivery systems provide a non-invasive alternative for delivering therapeutic agents across the skin, effectively bypassing gastrointestinal absorption and liver metabolism[23]. Compared to oral or injectable methods, transdermal drug delivery systems offer sustained drug release, enhance patient compliance, and reduce systemic side effects[24]. However, the primary challenge is the limited permeability of the stratum corneum, the dense outer layer of the skin that restricts the passage of hydrophilic or molecules with high molecular weight[25]. Various chemical and physical enhancement strategies have been explored to improve skin permeability, including the use of penetration enhancers, ultrasound, and innovative delivery platforms[26].

doi:10.6342/NTU202501655

1.4. Microneedle system

The microneedle system has garnered significant attention as a minimally invasive and highly effective method for enhancing transdermal drug delivery. Microneedles are tiny projections that painlessly penetrate the outermost layer of the skin, known as the stratum corneum, creating temporary microchannels[27]. These channels facilitate the diffusion of drugs into the deeper layers of the skin. This delivery method enables targeted treatment of specific skin areas while minimizing the impact on the rest of the body, making it particularly useful for addressing skin-related conditions[28]. Various types of microneedles have been developed, including solid, coated, hollow, dissolving, and hydrogel-forming formats (**Fig. 1.3**), each tailored to meet specific release profiles and therapeutic requirements[29]. Dissolving microneedles, in particular, are fabricated from biocompatible polymers that encapsulate active agents and dissolve upon insertion into skin, providing a safe and efficient delivery platform for both small molecules and macromolecules[29].

doi:10.6342/NTU202501655

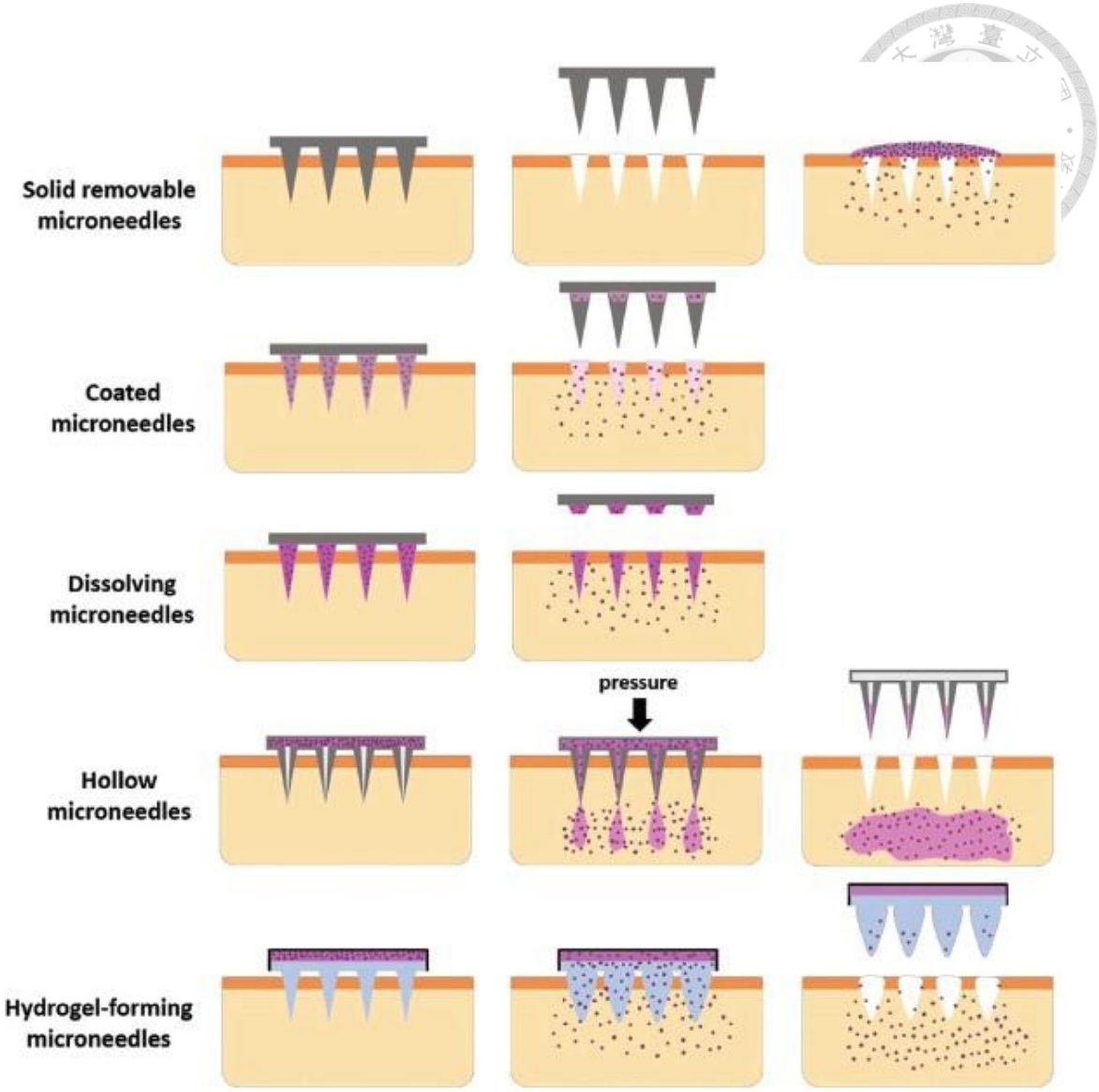

Fig. 1.3. Schematic illustration of different microneedle types and their respective drug delivery mechanisms[29].

doi:10.6342/NTU202501655

2. Literature Review

Biocompatible polymers are widely utilized in the fabrication of microneedles for transdermal drug delivery due to their adjustable mechanical strength, degradation profiles, and ease of processing[30]. Based on the drug release behavior, polymeric microneedles can be broadly classified into three functional types known as swelling, immediate-release, and sustained-release microneedles[31]. The choice of polymer is crucial in determining the release profile of the system, as the intrinsic and mechanical properties of each material influence drug diffusion, skin insertion, and structural integrity[32]. Below is a summary of commonly used polymers associated with each microneedle type (**Table 2.1**).

Swelling microneedles are made from hydrophilic polymers that absorb interstitial fluid upon insertion, expanding to form hydrogel-like structures that enable sustained or diffusion-controlled drug release[33]. Typical materials in this category include polyvinyl alcohol (PVA) and gelatin methacryloyl (GelMA). PVA is a synthetic, water-soluble polymer with a Young's modulus of 2.75 GPa and tensile strength of about 45 MPa[34]. While it dissolves slowly, its ability to swell and form a hydrogel matrix supports its classification as a swelling microneedle material. PVA is advantageous due to its biocompatibility, processability, and tunable swelling behavior in biological fluids[35].

doi:10.6342/NTU202501655

Similarly, GelMA, a photo-crosslinkable hydrogel has a lower Young's modulus of 3.08×10^{-6} GPa, allowing for customizable swelling kinetics and drug release rates[36].

Immediate-release microneedles are constructed from water-soluble polymers that dissolve rapidly upon contact with the skin, enabling quick drug release[37]. Materials such as carboxymethyl cellulose (CMC) fall into this category. CMC has a modulus of about 0.198 GPa and a tensile strength of around 27.5 MPa, providing sufficient stiffness while dissolving quickly[38]. These properties allow the material to support microneedle insertion when mechanical assistance is applied.

Sustained-release microneedles are designed to provide prolonged therapeutic effects by utilizing slowly degrading, hydrophobic polymers[39]. Key examples include polycaprolactone (PCL) and poly(lactic-co-glycolic acid) (PLGA). PCL has a Young's modulus ranging from 0.21 to 0.44 GPa and a tensile strength between 20.7 and 42 MPa, offering flexible yet durable insertion properties[40]. PLGA exhibits similar mechanical performance, with a Young's modulus of 1.4 to 2.8 GPa and a tensile strength of 41.4 to 55.2 MPa[40]. Their mechanical robustness allows for skin penetration without fracture while supporting gradual drug elution over days to weeks. However, these materials are not suitable for dissolving microneedles and require melt processing or organic solvents for fabrication.

doi:10.6342/NTU202501655

Overall, by aligning the characteristics of polymers with the desired therapeutic release profile, microneedle systems can be finely tuned for specific clinical needs[41]. Swelling systems using PVA allow for hydrogel-mediated release, while CMC enables rapid disintegration in immediate-release formats.

Table 2.1. Summary of mechanical strength of common polymeric materials for microneedles ('-' indicates data not reported in the literature).

Type	Typical material	Tensile strength (MPa)	Young's modulus (GPa)	Reference
Swelling microneedle	PVA	44±1.5	2.75	[34]
	PAA	-	1.31×10^{-5}	[42]
	Gelatin	-	7.5×10^{-5}	[43]
	GelMA	-	3.08×10^{-6}	[36]
Sustained-release microneedle	PLGA	41.4-55.2	1.4-2.8	[40]
	PCL	20.7-42	0.21-0.44	[40]
Immediate-release	PLA	59.903±4.92	3.986±0.421	[44]

doi:10.6342/NTU202501655

microneedle				
	CMC	27.5±2.5	0.198±0.18	[38]
	PVP	-	0.107	[45]

doi:10.6342/NTU202501655

3. Objective

This research aims to develop a biocompatible transdermal delivery system by integrating iron-based metal-organic frameworks (i.e., MIL-100(Fe)) into dissolvable microneedles for the treatment of skin fibrosis, a condition characterized by excessive collagen deposition and abnormal scar formation. The study focuses on synthesizing and characterizing MIL-100(Fe) particles that are suitable for biomedical applications. These particles will be incorporated into microneedle patches composed of polyvinyl alcohol (PVA) or sodium carboxymethyl cellulose (CMC). The research will examine the morphological uniformity, polymer compatibility, and mechanical strength of the microneedles to ensure effective skin penetration.

In addition, the cytocompatibility of MIL-100(Fe) will be evaluated using human keloid fibroblasts to confirm its biosafety and potential for long-term cutaneous application. The delivery performance of the system will also be investigated through *in vitro* permeation tests using porcine skin models to determine whether the therapeutic agents can reach the dermal layer. Through this work, a localized and minimally invasive strategy is proposed to address challenges associated with the treatment of fibrotic skin conditions.

doi:10.6342/NTU202501655

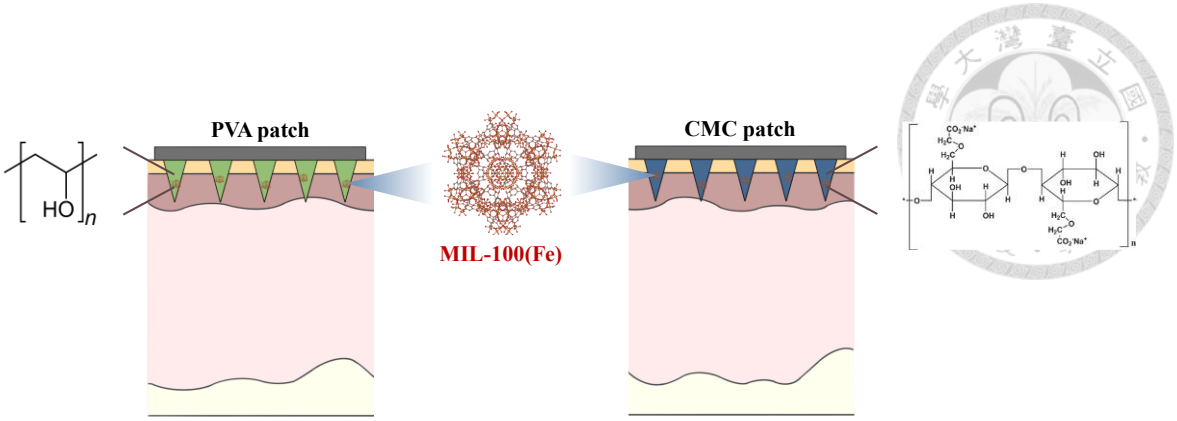

Fig. 3.1. The schematic objective of this work.

doi:10.6342/NTU202501655

4. Experimental

4.1. Materials

Table 4.1. Materials.

Chemical	Formula	Information
Iron(III) chloride hexahydrate	$FeCl_3 \cdot 6H_2O$	Sigma Aldrich
Benzene-1,3,5-tricarboxylic acid	$C_9H_6O_6$	Sigma Aldrich
Polydimethylsiloxane (PDMS)	$(C_2H_6OSi)_n$	Dow Corning
Sodium carboxymethyl cellulose (CMC)	$C_8H_{15}NaO_8$	MW=90000, Sigma Aldrich
Polyvinylpyrrolidone (PVP)	$(C_6H_9NO)_n$	MW=360000, Sigma Aldrich
Polyvinyl alcohol (PVA)	$(C_2H_4O)_n$	87-89% hydrolyzed, MW=85000-124000, Sigma Aldrich
Ethanol	C_2H_5OH	Honeywell
Hexane	C_6H_{14}	Macron
1,1,1,3,3,3-Hexafluoro-	$C_3H_2F_6O$	≥ 99%, Sigma Aldrich

doi:10.6342/NTU202501655

2-propanol		
Rhodamine 6G	$C_{28}H_{31}N_2O_3Cl$	~95%, Sigma Aldrich
Dulbecco's Modified Eagle Medium (DMEM)	N/A	Gibco
Fetal bovine serum (FBS)	N/A	Thermo Fisher Scientific
L-glutamine	$C_5H_{10}N_2O_3$	Gibco
Sodium pyruvate	$NaC_3H_3O_3$	Gibco
Antibiotic-antimycotic	N/A	Gibco
Phosphate-buffered saline (PBS)	N/A	10×, Gibco
Trypsin	N/A	10×, Gibco
AlamarBlue	N/A	Gibco

doi:10.6342/NTU202501655

4.2. Equipment

Table 4.2. List of equipment.

Equipment	Manufacturer
X-ray diffractometer (XRD)	Rigaku MiniFlex
Dynamic light scattering (DLS)	Malvern, Zetasizer Nano ZS
Specific surface area	BELSORP-max II
Cold-field emission scanning electron microscope (CFE SEM)	Hitachi, S-4800
Transmission electron microscope (TEM)	Hitachi, H7100
Multimode Reader	Biotek, Synergy HTX
Optical microscope (OM)	SOPTOP SZN71
Confocal laser scanning microscope (CLSM)	ZEISS, LSM 900
Incubator	NUAIRE, NU-5810U-SSRG
Open circulating bath	FIRSTEK, B206
Dynamic mechanical analysis (DMA)	TA Instruments, Q800
Centrifugator	Himac, CT18R
Sonicator	DELTA
Vacuum pump	KNF, N840 Laboport
Hotplate	Thermal Scientific

doi:10.6342/NTU202501655

Lab Water Purification Systems	ELGA, PURELAB Classic
Lyophilizer	EYELA, FDU-1200
3D Printer	FreEntity, F2

doi:10.6342/NTU202501655

4.3. Cell line

Primary human keloid fibroblasts were obtained from Chang Gung Memorial Hospital (Linkou, Taiwan). The cells were cultured in Dulbecco's Modified Eagle Medium (DMEM) supplemented with 10% fetal bovine serum (FBS), 1% L-glutamine, 1% sodium pyruvate, and 1% antibiotic-antimycotic solution.

4.4. Statistical analysis

Statistical analysis was conducted using OriginLab Origin 2025 and Microsoft Excel. Results are expressed as mean ± standard deviation (SD), with the number of replicates (N) indicated in the respective figure captions.

4.5. Synthesis of MIL-100(Fe)

MIL-100(Fe) was synthesized via a microwave-assisted hydrothermal method, based on the procedure reported by Marquez et al. (2012). To begin, iron(III) chloride hexahydrate ($FeCl_3 \cdot 6H_2O$) (0.2162 g, 0.8 mmol) and benzene-1,3,5-tricarboxylic acid (H_3BTC) (0.1125 g, 0.54 mmol) were added to 20 mL of deionized water (DI water) in a reaction vial. The mixture was then transferred to the microwave reactor and pre-stirred for 5 min. Subsequently, the mixture was heated to 130°C for 6 min. Upon completion of

doi:10.6342/NTU202501655

the reaction, the product was allowed to cool to room temperature. The as-formed orange-colored suspension was collected and washed twice with water and twice with ethanol through centrifugation (15,000 rpm, 10 min). After washing, the orange precipitate, identified as MIL-100(Fe), was re-suspended in DI water for subsequent applications (**Fig. 4.1**).

Fig. 4.1. Schematic illustration of the synthesis procedure for MIL-100(Fe).

4.6. Microneedle patches

4.6.1. 3D-printed mold

The master molds of the microneedle patches were designed using Rhinoceros 3D modeling software. The design files were exported in .stl format and provided to FreEntity Co., Ltd. (New Taipei, Taiwan) for 3D printing of the master molds (**Fig. 4.2**).

doi:10.6342/NTU202501655

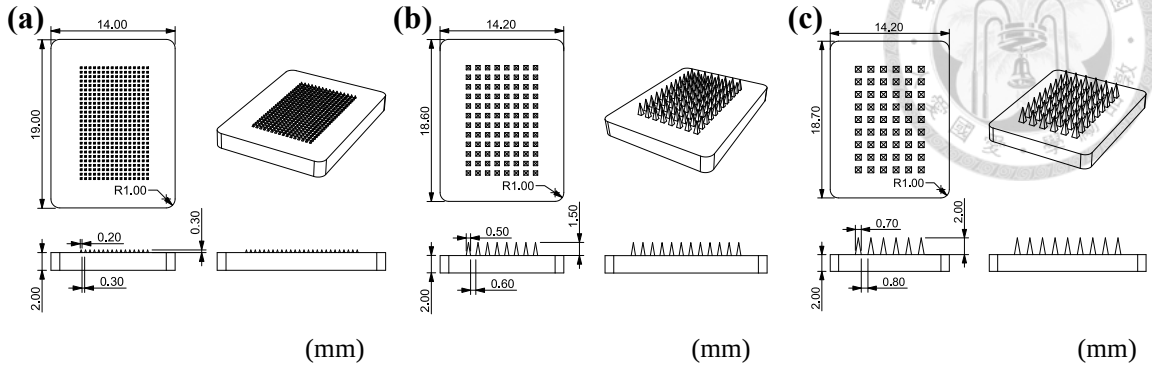

Fig. 4.2. Technical drawings of microneedle patch molds with needle lengths of (a) 0.3 mm, (b) 1.5 mm, and (c) 2.0 mm.

4.6.2. Resin container

A resin container was designed to centrally position the microneedle master mold, enabling the addition and curing of PDMS to produce a negative mold. The container was modeled using Rhinoceros 3D software, and the design files were exported in .stl format for 3D printing using UV-curable resin (**Fig. 4.3**).

doi:10.6342/NTU202501655

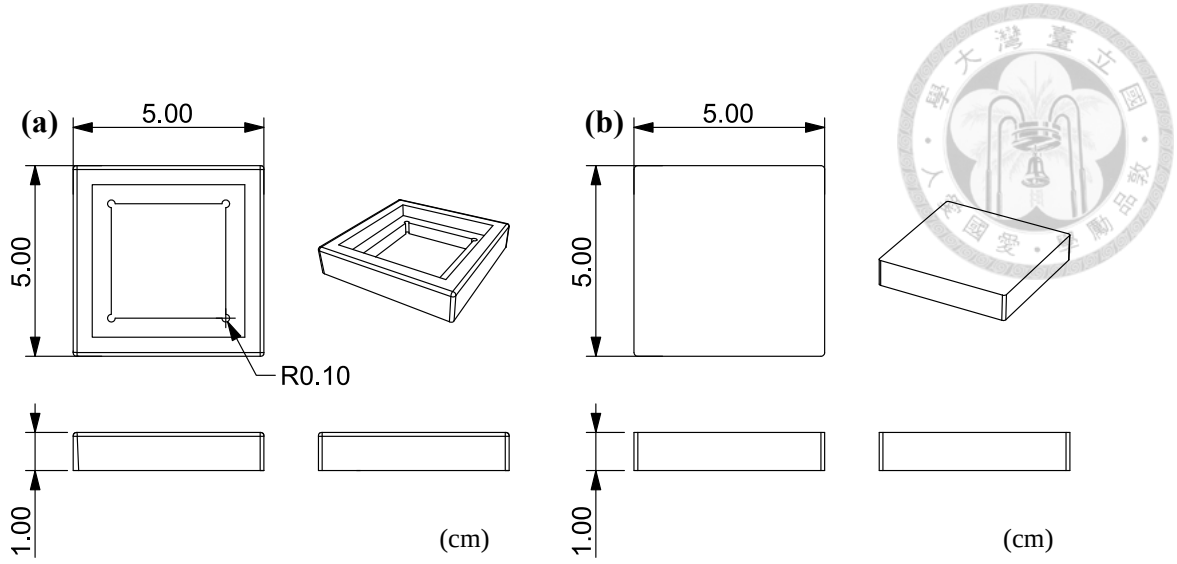

Fig. 4.3. Technical drawings of the (a) upper part and (b) lower part of the resin container components.

4.6.3. PDMS mold

Polydimethylsiloxane (PDMS) was used to fabricate the negative molds for the microneedle patches. Reagent A and reagent B were mixed at a 10:1 weight ratio and thoroughly blended. The mixture was then degassed in a vacuum desiccator to remove air bubbles. The 3D-printed master mold was placed at the center of the resin container, and the PDMS mixture was poured in. A second round of degassing was performed before allowing the setup to cure at room temperature for approximately three days. Once cured, the PDMS mold was trimmed using a scalpel to fit the dimensions of a centrifuge tube. The 3D-printed molds and resin container were subsequently cleaned with hexane.

doi:10.6342/NTU202501655

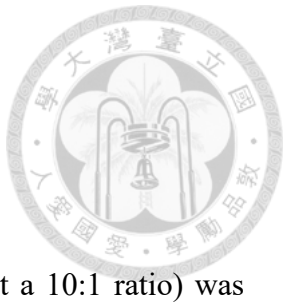

4.6.4. Centrifuge tube

Approximately 7 mL of a PDMS mixture (reagents A and B at a 10:1 ratio) was poured into a centrifuge tube and allowed to cure, forming a solid base. This cured PDMS platform provided structural support for positioning the PDMS negative mold inside the tube, facilitating centrifugation in subsequent experiments.

4.6.5. General procedure for fabricating microneedle patches

Polymer solutions of 7 wt% polyvinyl alcohol (PVA) or sodium carboxymethyl cellulose (CMC), typically stored at 4°C, were thawed by heating on a hot plate at 50°C. The PDMS negative mold was then horizontally positioned in a centrifuge tube using forceps. The thawed polymer solution was added to the mold, and the setup was subjected to centrifugation (4,000 rpm, 20 min) to facilitate the filling of the microneedle cavities. After centrifugation, the mold was carefully removed using forceps, and the excess polymer solution was scraped off with a spatula. The mold was then placed in a Petri dish and left to dry at room temperature in a hood overnight.

To form the backing layer of the microneedle patch, a solution consisting of 8 wt% CMC and 2 wt% polyvinylpyrrolidone (PVP), also stored at 4°C, was thawed at 60°C

doi:10.6342/NTU202501655

using a hot plate. The dried PDMS negative mold was repositioned in a centrifuge tube, and the thawed backing solution was poured into the mold. The mold was then centrifuged (4,000 rpm, 20 min) to remove air bubbles and ensure uniform layer formation. Following centrifugation, the mold was gently retrieved with forceps and placed in a Petri dish to dry under ambient conditions in the hood for 2 to 3 days.

Once the microneedle patch was fully dried, it was carefully demolded from the PDMS negative mold.

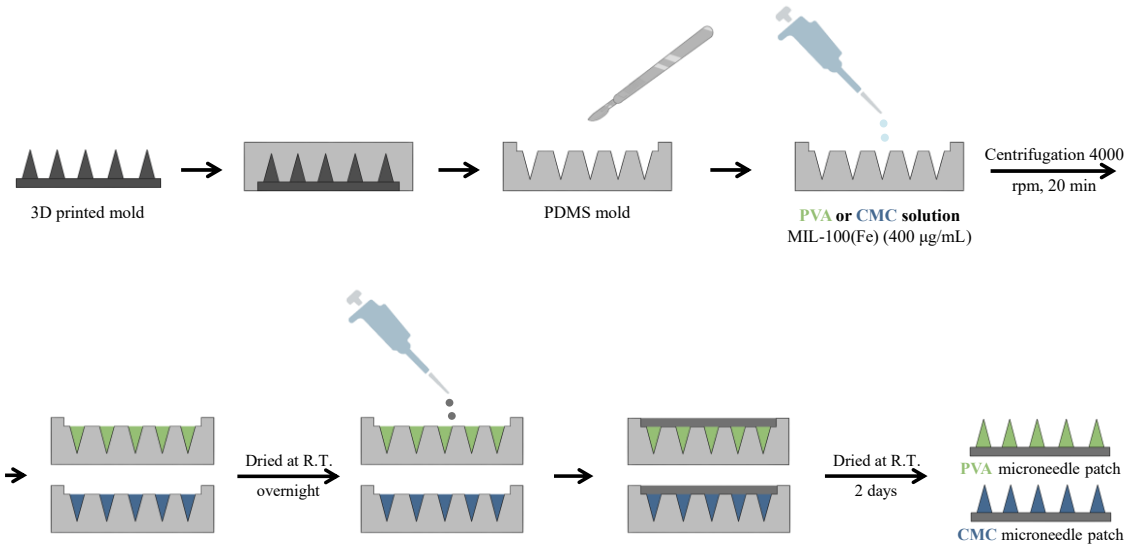

Fig. 4.4. Schematic illustration of the fabrication process for the microneedle patch.

4.6.6. Washing process for PDMS negative molds

The PDMS negative molds were cleaned by sonication in approximately 20 mL of 1,1,1,3,3,3-hexafluoro-2-propanol within a serum bottle for 15 min. This was followed

doi:10.6342/NTU202501655

by sonication using dish detergent for another 15 min. The molds were then rinsed by sonicating twice in deionized water, each for 15 min. After cleaning, the molds were dried overnight in an oven at 60°C. Each PDMS negative mold could be reused up to about 20 times.

4.6.7. *In vitro* test for drug release depth in porcine skin

Porcine skin used in this experiment was sourced from a local butcher and pretreated by removing hair and excess subcutaneous fat. The skin was stored at -20°C until use. While still frozen, it was trimmed to match the dimensions of the microneedle patch. Thawing was performed by rinsing the skin under running tap water. After thawing, an exfoliating cream was applied to the skin surface to enhance cleanliness and uniformity, then rinsed off with water, and the skin was gently dried with paper towels.

A microneedle patch pre-stained with Rhodamine 6G (15 mg/mL) was prepared by trimming its edges with scissors to ensure a neat fit. The patch was then applied to the porcine skin using a dynamic mechanical analyzer (DMA) under a constant force of 12 N to ensure consistent insertion. Following application, the porcine skin was re-frozen and subsequently sectioned into thin slices for imaging. Confocal laser scanning microscopy (CLSM) was used to visualize the insertion and distribution of the

doi:10.6342/NTU202501655

microneedle patch.

4.7. Characterization

4.7.1. X-ray diffractometer (XRD)

The crystal structures of the materials were characterized by conducting powder X-ray diffraction (PXRD) using a Miniflex X-ray diffractometer from Rigaku (Tokyo, Japan) equipped with Cu Kα radiation (λ = 1.5418 Å). Specific measurement parameters are summarized in **Table 4.3**.

Table 4.3. The detailed measurement parameters of XRD.

Parameters	Value
X-ray source	Cu Kα
Wavelength (λ)	1.5418 Å
Voltage	40 kV
Current	40 mA
Angle range	1°-70°
Time per step	0.01 s

doi:10.6342/NTU202501655

Scanning rate	5°/min

4.7.2. Dynamic light scattering (DLS)

MIL-100(Fe) was dispersed in water by sonication and analyzed using a Zetasizer Nano ZS (Malvern, UK) to determine its particle size distribution.

4.7.3. Specific surface area

The N_2 adsorption isotherms for MIL-100(Fe) were measured using a BELSORP MAX II instrument from Microtrac Retsch GmbH (Haan, Germany). The specific surface area was evaluated using the Brunauer-Emmett-Teller Surface Identification (BETSI) method, a recently proposed refinement of the BET method, with version 2.0 of the BETSI software obtained from GitHub (https://github.com/fairen-group/betsi-gui). The analysis employed the following criteria: (1) a minimum of 3 data points in the linear region; (2) a coefficient of determination (R^2) of at least 0.999; and (3) all of Rouquerol's criteria were met. The software also automatically discarded data points with negative pressures or non-monotonic increases to ensure reliable results.

doi:10.6342/NTU202501655

4.7.4. Cold-field emission scanning electron microscope (CFE-SEM)

For SEM analysis of MIL-100(Fe), the powder samples were first dispersed in ethanol and drop-cast onto silicon wafers. The silicon wafers with the samples were fixed onto the sample stage using conductive carbon tape and placed in a vacuum oven overnight to eliminate residual moisture. Prior to imaging, the samples were sputter-coated using a Q150R S sputter coater equipped with a platinum target from Quorum (Laughton, UK). The SEM images were obtained using a Hitachi S-4800 cold-field emission SEM (Tokyo, Japan) operated at an acceleration voltage of 10 kV.

4.7.5. Transmission electron microscope (TEM)

A suspension of MIL-100(Fe) powder in ethanol was prepared and deposited onto a copper grid. The transmission electron microscope (TEM) images of the materials were acquired using a Hitachi H7100.

4.7.6. Optical microscope (OM)

Microneedle patches were secured onto the self-made plastic stage using 3M adhesive tape. The optical microscope (OM) images of the microneedle patches were captured using SOPTOP SZN71 (Ningbo, China).

doi:10.6342/NTU202501655

4.7.7. Cytotoxicity assay

The cytotoxicity of the materials was evaluated with the AlamarBlue^{TM} assay (**Fig. 4.5**), which assesses cellular metabolic activity by measuring the reduction of resazurin to resorufin, serving as an indicator of mitochondrial function and overall cell viability. Human keloid fibroblasts (8×10^3 cells in 100 μL of complete culture medium) were seeded into the wells of a 96-well plate and incubated at 37°C in a 5% CO_2 incubator. The next day, the medium was replaced with 100 μL of fresh complete medium containing test materials at concentrations ranging from 0 to 500 μg/mL. The cells were incubated for 24 h. Subsequently, 90 μL of complete culture medium and 10 μL of AlamarBlue reagent were added to each well. After a 4-hour incubation, absorbance at 570 nm was recorded using a Multimode Reader from Biotek. The background readings were corrected by subtracting readings from wells containing medium, materials, and AlamarBlue reagent, but without cells.

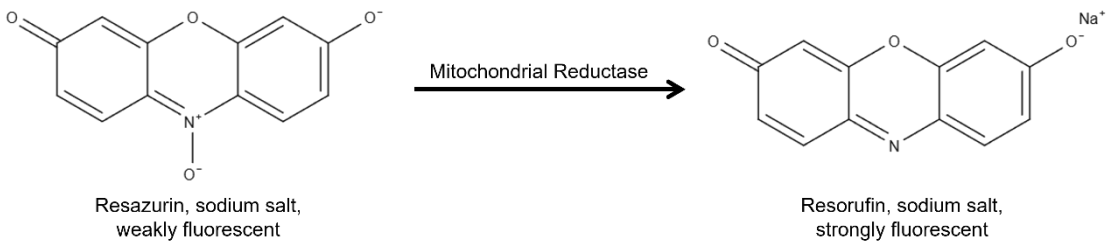

Fig. 4.5. The mechanism of the AlamarBlue assay experiment.

doi:10.6342/NTU202501655

The relative viabilities of the cells were then calculated using **Equation 4.1**:

$$\text{Relative Viability (\%)} = \frac{FI_{Sample}}{FI_{Control}} \times 100\% \quad \textbf{(4.1)}$$

4.7.8. Dynamic mechanical analysis (DMA)

CMC or PVA was dissolved in deionized water and stirred at 50°C to obtain homogeneous solutions. The prepared solutions were transferred into 15 mL centrifuge tubes and subjected to freeze-drying using an FDU-1200 lyophilizer from EYELA (Tokyo, Japan). After lyophilization, the resulting solid samples were carefully removed and shaped into cylindrical specimens with a diameter of 11 mm and a height of 0.8 mm using a scalpel. Compression testing was performed using a Q800 dynamic mechanical analyzer (DMA) from TA Instruments (New Castle, USA) to generate stress-strain curves.

The Young's modulus of both CMC and PVA was calculated based on **Equation 4.2**:

$$\text{Young's modulus (E, kPa)} = \frac{\text{Stress } (\sigma, \text{kPa})}{\text{Strain } (\varepsilon, \%)} \quad \textbf{(4.2)}$$

doi:10.6342/NTU202501655

4.7.9. Confocal laser scanning microscope (CLSM)

Thin slices of porcine skin were prepared using a scalpel and carefully placed in a Petri dish with a diameter of 3.5 cm. Confocal laser scanning microscopy (CLSM) images of the samples were obtained using the LSM 900 from ZEISS (Oberkochen, Germany).

doi:10.6342/NTU202501655

5. Results and Discussion

5.1. Synthesis and characterization of MIL-100(Fe)

A simplified method for synthesizing MIL-100(Fe) without the use of hydrofluoric acid, a commonly used but toxic mineralization agent, was recently developed[46], enabling a more biocompatible synthesis process. To control the particle size of MIL-100(Fe), we utilized a microwave reactor, which promotes rapid nucleation and results in smaller particle sizes. Consequently, MIL-100(Fe) was successfully synthesized, consisting of iron clusters linked by benzene-1,3,5-tricarboxylic acid (**Fig. 5.1**).

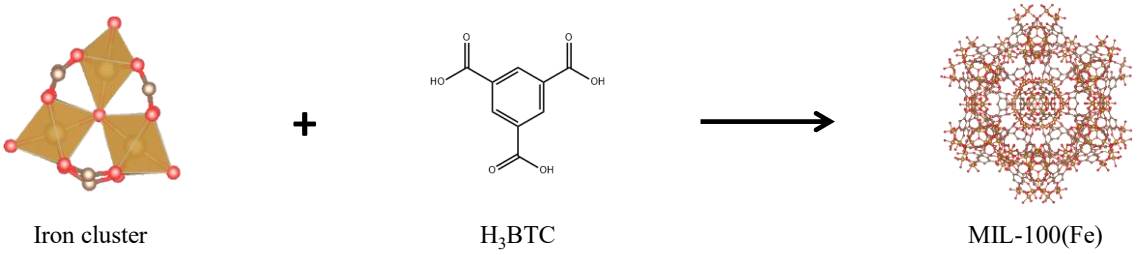

Fig. 5.1. The structure of MIL-100(Fe).

The X-ray diffraction (XRD) patterns of the as-synthesized MIL-100(Fe) are compared to the simulated pattern from the Crystallography Open Database (7102029) in **Fig. 5.2**. The characteristic peaks observed in the as-synthesized MIL-100(Fe) appear at 2.15°, 3.45°, 4.05°, 10.34°, and 10.88°, corresponding to the crystal planes (1 1 1), (2 2 0), (3 1 1), (8 2 2), and (9 1 1), respectively. These peaks align well with the simulated

doi:10.6342/NTU202501655

pattern, confirming the successful formation of the MIL-100(Fe) framework. However, the diffraction peaks of the as-synthesized sample show significant broadening and reduced intensity compared to the simulated MIL-100(Fe) pattern. This indicates a relatively lower degree of crystallinity, likely due to rapid nucleation during the synthesis process. No additional peaks were observed in the XRD pattern, indicating that the synthesized MIL-100(Fe) is pure in phase and free from detectable impurities, such as unreacted organic linker residues. Therefore, despite reduced crystallinity, the material retains the essential framework structure required for functional applications. Overall, the XRD results demonstrate that MIL-100(Fe) was successfully formed, although with lower crystallinity compared to the ideal structure. The crystallinity and structural characteristics of the sample were compared with findings from previous studies. Meta Angeine et al. synthesized MIL-100(Fe) using a hydrothermal method[47], which produced materials that displayed sharper and more intense diffraction peaks than those observed in this study. Their results suggest that extending the reaction time and maintaining controlled hydrothermal conditions can significantly enhance crystallinity. In contrast, Bac Thanh Le et al. utilized an ultrasonic-assisted method to fabricate MIL-100(Fe)[48], resulting in broader diffraction peaks and weaker intensities, similar to the observations made in this research. They attributed the decreased crystallinity to the rapid

doi:10.6342/NTU202501655

nucleation and accelerated crystal growth caused by ultrasonic irradiation, which restricts the time available for forming an ordered framework.

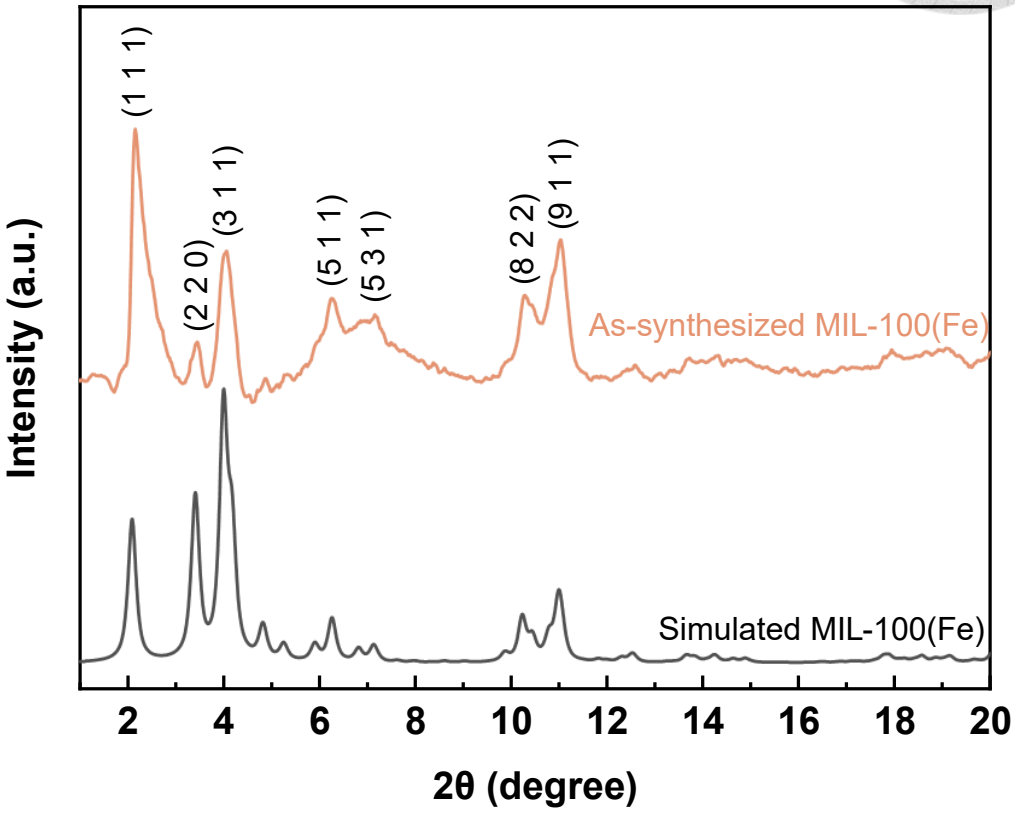

Fig. 5.2. The XRD patterns of MIL-100(Fe) and the simulated MIL-100(Fe).

The shape and structure of the MIL-100(Fe) particles synthesized by microwave-assisted hydrothermal methods were observed using SEM and TEM. The SEM image displayed the morphology of the MIL-100(Fe) as shown in **Fig. 5.3a**. However, the super-tetrahedral structure of MIL-100(Fe) was not clearly visible in the SEM image. This lack of clarity may be attributed to the rapid nucleation that occurs during microwave synthesis.

doi:10.6342/NTU202501655

The particle size is approximately estimated to be around 100 nm. The TEM image showed the aggregated structure of MIL-100(Fe), and the uniform contrast in the image indicates a relatively dense structure overall (**Fig. 5.3b**). When compared with previous studies by Meta Angeine et al. and Bac Thanh Le et al.[47, 48], our MIL-100(Fe) particles exhibited lower crystallinity. This difference is likely attributable to the rapid and uniform heating achieved through microwave synthesis, which promotes the formation of smaller particles.

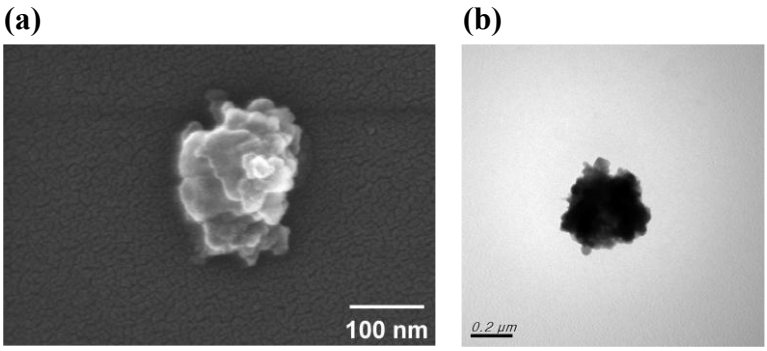

Fig. 5.3. The (a) SEM and (b) TEM images of MIL-100(Fe).

The N_2 adsorption/desorption isotherms of MIL-100(Fe) are presented in **Fig. 5.4**. The initial steep uptake at low relative pressures ($P/P_0 < 0.1$) suggests the presence of micropores. The BET surface area of the sample was calculated to be 949 m^2/g, which remains within the typical range reported for MIL-100(Fe) materials (800-1600 m^2/g).

Fig. 5.5 shows the BETSI result of MIL-100(Fe). The BET specific surface area of

doi:10.6342/NTU202501655

MIL-100(Fe) was determined to be 949 m^2/g, calculated from the linear region of the BET plot. The selection of the linear fitting range was validated by the Rouquerol plot, which showed a strong linearity in the selected region, with an R^2 value of 0.9995, confirming the reliability of the BET analysis.

When compared to previous reports, this surface area falls within the expected range for MIL-100(Fe). For instance, Meta Angeine et al. synthesized MIL-100(Fe) using a hydrothermal method[47], reporting a BET surface area of 1350 m^2/g, attributed to well-developed crystallinity and open porosity. In another study, Bac Thanh Le et al. employed an ultrasonic-assisted method to prepare MIL-100(Fe) as a drug carrier[48], resulting in a BET surface area of 846 m^2/g. These variations are often linked to differences in synthesis techniques, particle size, defect density, and activation protocols.

doi:10.6342/NTU202501655

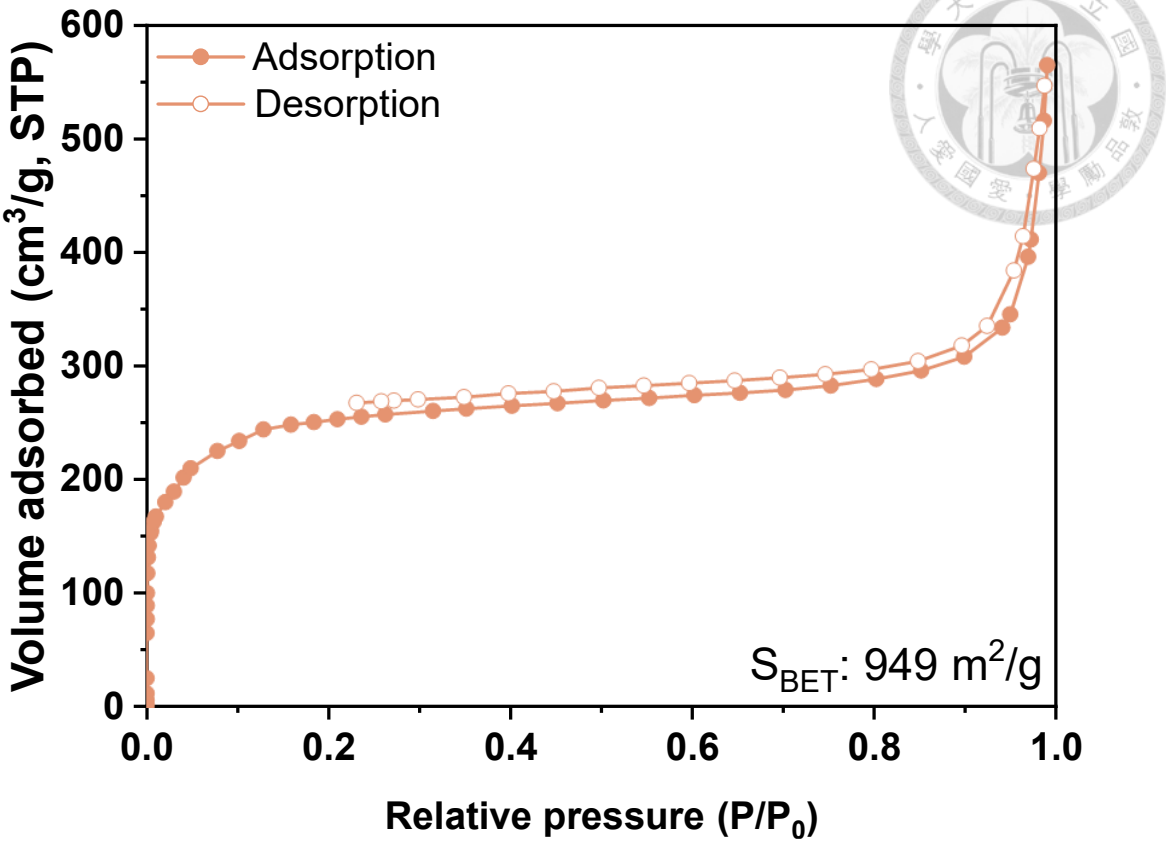

Fig. 5.4. The N_2 adsorption and desorption isotherms of MIL-100(Fe).

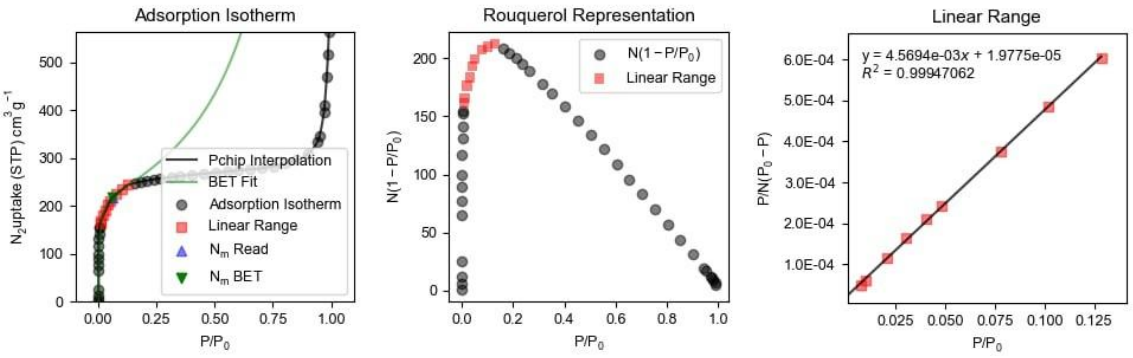

Fig. 5.5. Applying the BETSI method to identify the suitable range for calculating the specific surface area of MIL-100(Fe).

doi:10.6342/NTU202501655

The DLS analysis of the synthesized MIL-100(Fe) nanoparticles revealed a Z-average hydraulic diameter of 178.5 ± 6.0 nm with a low polydispersity index (PDI) of 0.151 ± 0.025, based on three independent measurements (N=3) (**Fig. 5.6**). The narrow size distribution and low PDI value indicate that the particles exhibit a relatively uniform and well-dispersed in water. The slightly larger hydraulic diameter compared to the particle size observed in SEM and TEM images can be attributed to the presence of surrounding solvent layers during DLS measurement. The low PDI (< 0.3) also suggests that the nanoparticles have good colloidal stability, which is important for further applications. In comparison to previous studies, our synthesized MIL-100(Fe) nanoparticles displayed a smaller hydraulic size of 178.5 ± 6.0 nm and a lower PDI value of 0.151 ± 0.025 than the MIL-100(Fe) nanoparticles prepared using the hydrothermal method[49]. These findings indicate that the microwave-assisted approach utilized in our research promotes the formation of smaller and more uniform MIL-100(Fe) nanoparticles. This characteristic could be beneficial for applications that depend on enhanced dispersion or improved cellular uptake.

doi:10.6342/NTU202501655

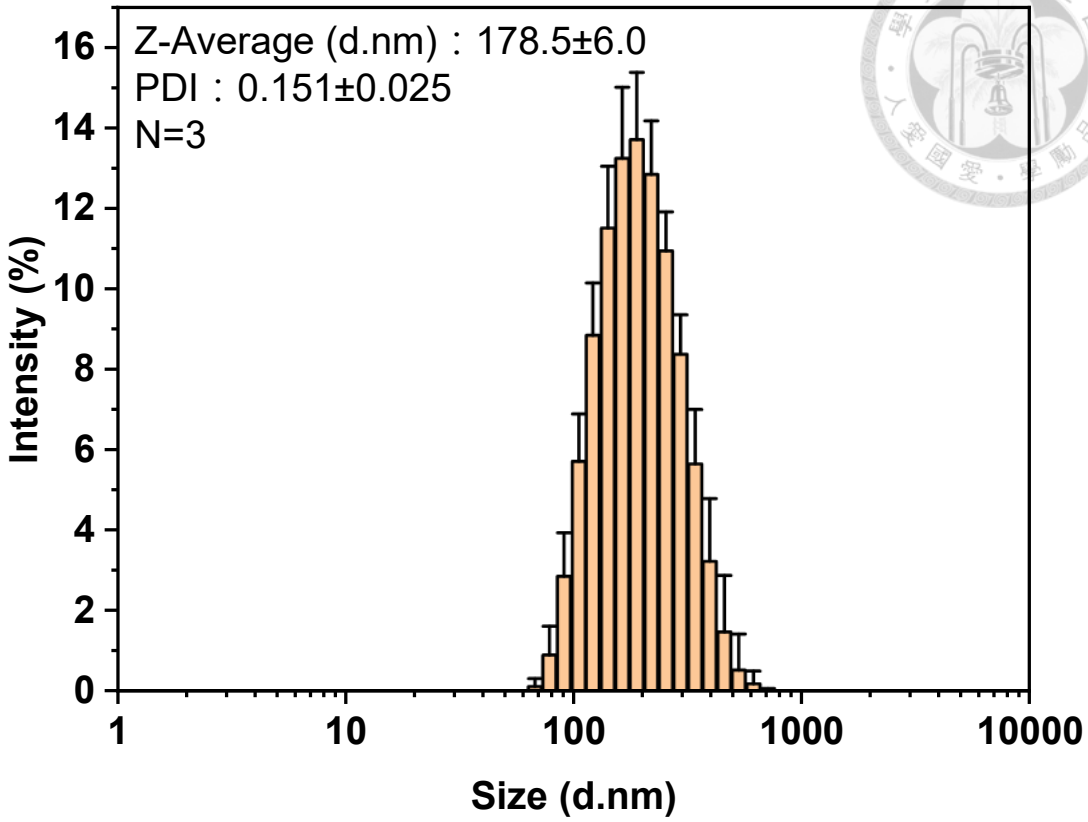

Fig. 5.6. The DLS results of MIL-100(Fe) (N=3).

5.2. Biocompatibility of MIL-100(Fe)

The cytotoxicity of MIL-100(Fe) on human keloid fibroblasts was evaluated using the AlamarBlue assay after 24 h of incubation. As shown in **Fig. 5.7**, cell viability remained above 90% across all tested concentrations (10-500 μg/mL), indicating low cytotoxicity. No significant cytotoxicity was observed at concentrations up to 200 μg/mL, with cell viability comparable to the untreated control (0 μg/mL). However, at 500 μg/mL, there was a slight but statistically significant decrease in viability ($p < 0.05$), indicating

doi:10.6342/NTU202501655

minimal cytotoxicity at higher doses. Despite this decline, overall viability remained high (> 90%), suggesting that MIL-100(Fe) exerts minimal toxic effects on human keloid fibroblasts within this concentration range. These results suggest that MIL-100(Fe) exhibits excellent biocompatibility at concentrations up to 200 μg/mL, with no significant reduction in cell metabolic activity, as indicated by the AlamarBlue assay. The assay measures the reduction of resazurin to resorufin, which reflects mitochondrial function and overall cell health. Although the decline in viability at 500 μg/mL was statistically significant, it still maintained above 90% viability, suggesting that the material is largely safe for biomedical applications at this level. The observed dose-dependent response aligns with typical cellular tolerance thresholds, supporting the feasibility of using MIL-100(Fe) in transdermal or localized drug delivery systems without inducing severe cytotoxic effects.

Our findings are consistent with previous reports. For instance, one study evaluated the cytotoxicity of MIL-100(Fe) using the MTT assay on human liver cells (HL-7702) and liver cancer cells (HepG2), and reported that concentrations below 80 μg/mL resulted in cell viability above 85%, indicating good biocompatibility[50]. Another study also demonstrated that MIL-100(Fe)-based nanocarriers exhibited low cytotoxicity across various cell lines[20], further confirming the biocompatibility of this metal-organic

doi:10.6342/NTU202501655

framework (MOF). Although that work primarily focused on their application in photodynamic therapy, the material properties examined are consistent with the cytotoxicity trends observed in our study. These results consistently demonstrate the biocompatibility of MIL-100(Fe) across various cell types and synthesis methods, highlighting its potential as a safe candidate for biomedical applications, particularly for the localized treatment of fibrotic or scarred tissues.

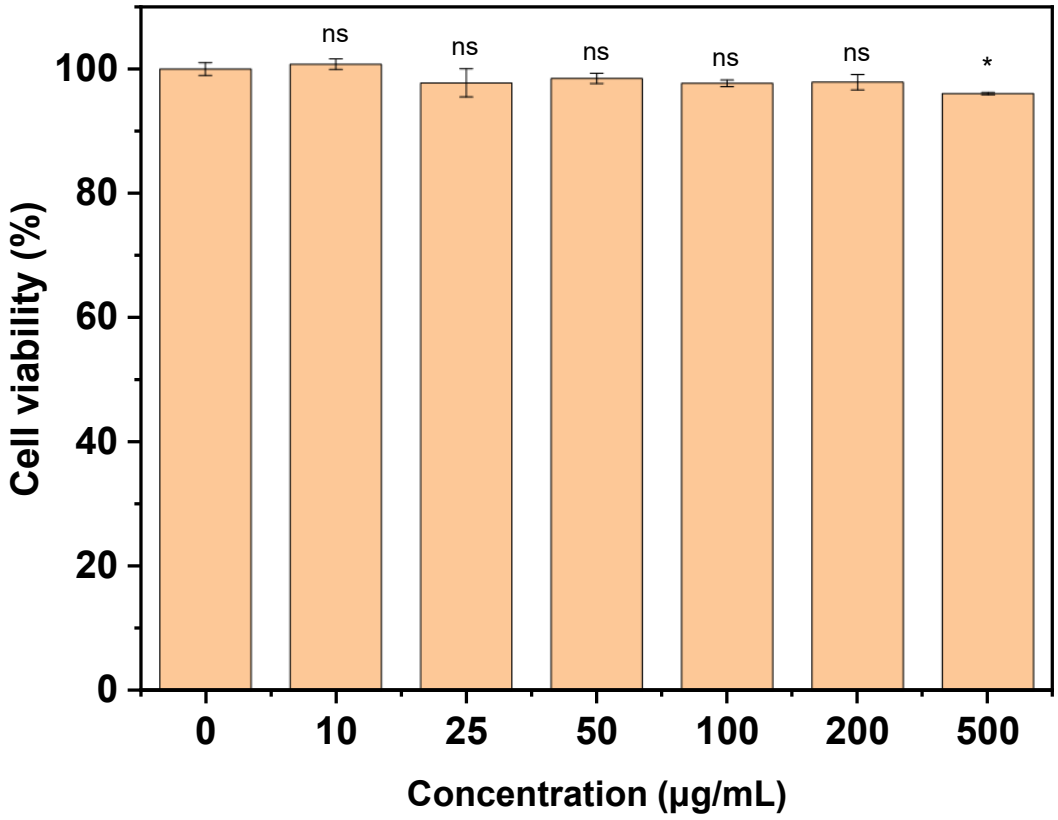

Fig. 5.7. The relative viability of human keloid fibroblast cells after 24 h of incubation with MIL-100(Fe). Data are mean ± standard deviation (N=3). Statistical comparisons were made between the control and each treatment group using an unpaired two-tailed

doi:10.6342/NTU202501655

Student’s t-test. ns: non-significant, *p ≤ 0.05.

5.3. Young’s modulus of the needle part of the microneedle patch

Dynamic mechanical analysis was performed to evaluate the mechanical performance of CMC and PVA at various concentrations, with the stress-strain behavior recorded for each sample. The slope of the linear region in each curve was used to calculate the Young’s modulus, providing a quantitative measure of stiffness. As shown in the stress-strain curves, the mechanical strength increased with polymer concentration for both materials, although the trends differed between CMC and PVA (**Fig. 5.8**).

For CMC, the mechanical behavior exhibited a nearly linear elastic response, suggesting stable deformation under applied stress. The Young's modulus increased significantly from 0.754 kPa at a concentration of 3 wt% to 8.245 kPa at 7 wt%, indicating that higher concentrations notably enhanced the stiffness of the material (**Table 5.1**). This improvement can be attributed to the denser polymer network formed at higher concentrations, which offers greater resistance to deformation. In contrast, PVA displayed a relatively nonlinear stress-strain profile, showing progressively higher stiffness with increased concentrations. Although the highest modulus was recorded at 13 wt% (7.197 kPa), this concentration was associated with a notable reduction in strain tolerance,

doi:10.6342/NTU202501655

potentially compromising flexibility during microneedle application. While higher concentrations of PVA do provide improved mechanical strength, material characteristics such as viscosity, moldability, and drying behavior must also be considered for practical microneedle fabrication. Therefore, 7 wt% PVA was selected to match the CMC concentration, allowing for a fair comparison in subsequent experiments. This concentration exhibited a moderate Young's modulus of 2.661 kPa, ensuring a balance between mechanical integrity and material handling properties.

To further evaluate the functional performance of both materials, 7 wt% formulations of CMC and PVA were selected for microneedle fabrication and will be directly compared in an *in vitro* porcine skin penetration experiment. This direct comparison at equal concentrations will facilitate a clearer assessment of material-dependent penetration efficiency and mechanical reliability under simulated transdermal conditions.

doi:10.6342/NTU202501655

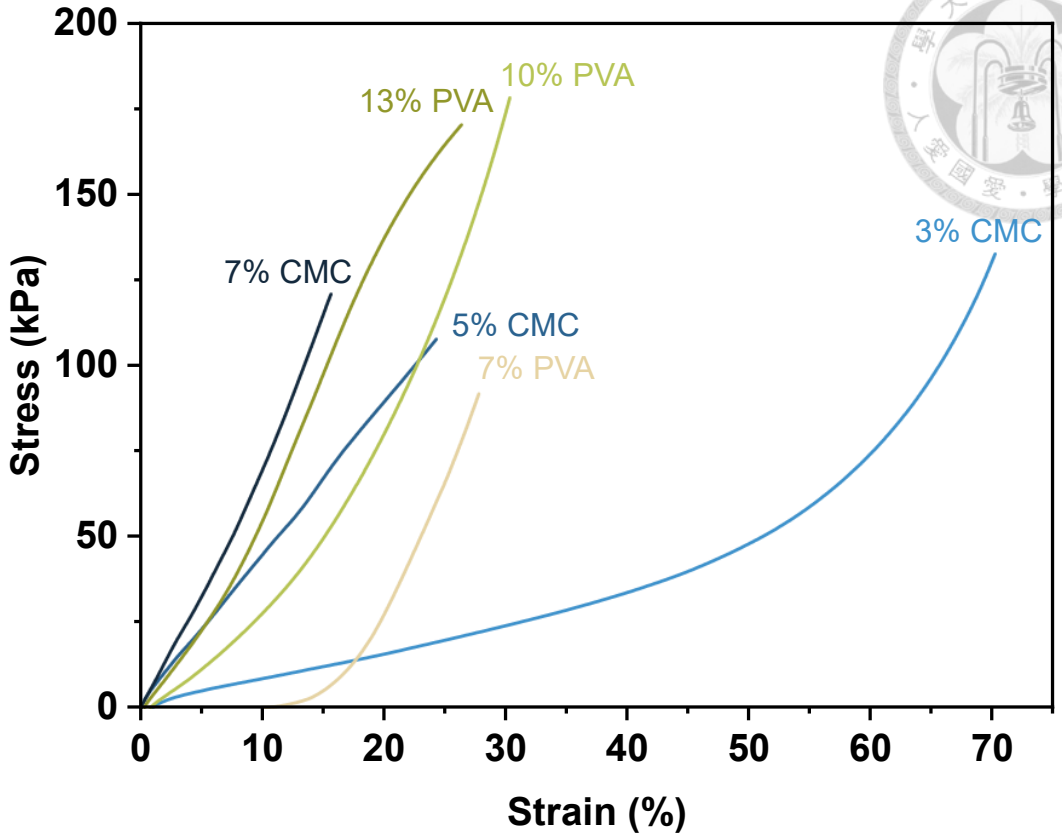

Fig. 5.8. DMA results of CMC (3, 5, and 7 wt%) and PVA (7, 10, and 13 wt%), showing stress-strain profiles used to evaluate mechanical properties for microneedle design.

Table 5.1. Young's modulus values of sodium carboxymethyl cellulose (CMC) and polyvinyl alcohol (PVA) at various concentrations (wt%) as determined from DMA measurements.

Material	Concentration (wt%)	Young's modulus (kPa)
Sodium carboxymethyl cellulose (CMC)	3	0.754

doi:10.6342/NTU202501655

	5	4.415
	7	8.245
Polyvinyl alcohol (PVA)	7	2.661
	10	3.126
	13	7.197

5.4. Morphology of the microneedle patch

Microneedle patches were fabricated using 7 wt% PVA or 7 wt% CMC with needle lengths of 0.3 mm, 1.5 mm, and 2.0 mm, with the needle part encapsulated with 400 μg/mL MIL-100(Fe). Their structural features were evaluated under optical microscopy, and all of them were shown with and without rhodamine 6G staining. The images were captured from multiple viewing angles, including top view (10× and 30×), oblique view (30×), and side view (30×), to assess overall geometry, tip sharpness, and vertical alignment.

5.4.1. Microneedle patches composed of 7 wt% PVA with a needle length of 0.3 mm

The 0.3 mm microneedles were well-formed and consistent in shape. All needles

doi:10.6342/NTU202501655

were uniformly arranged, sharply tapered, and vertically oriented, with no evidence of collapse or fusion (**Fig. 5.9**).

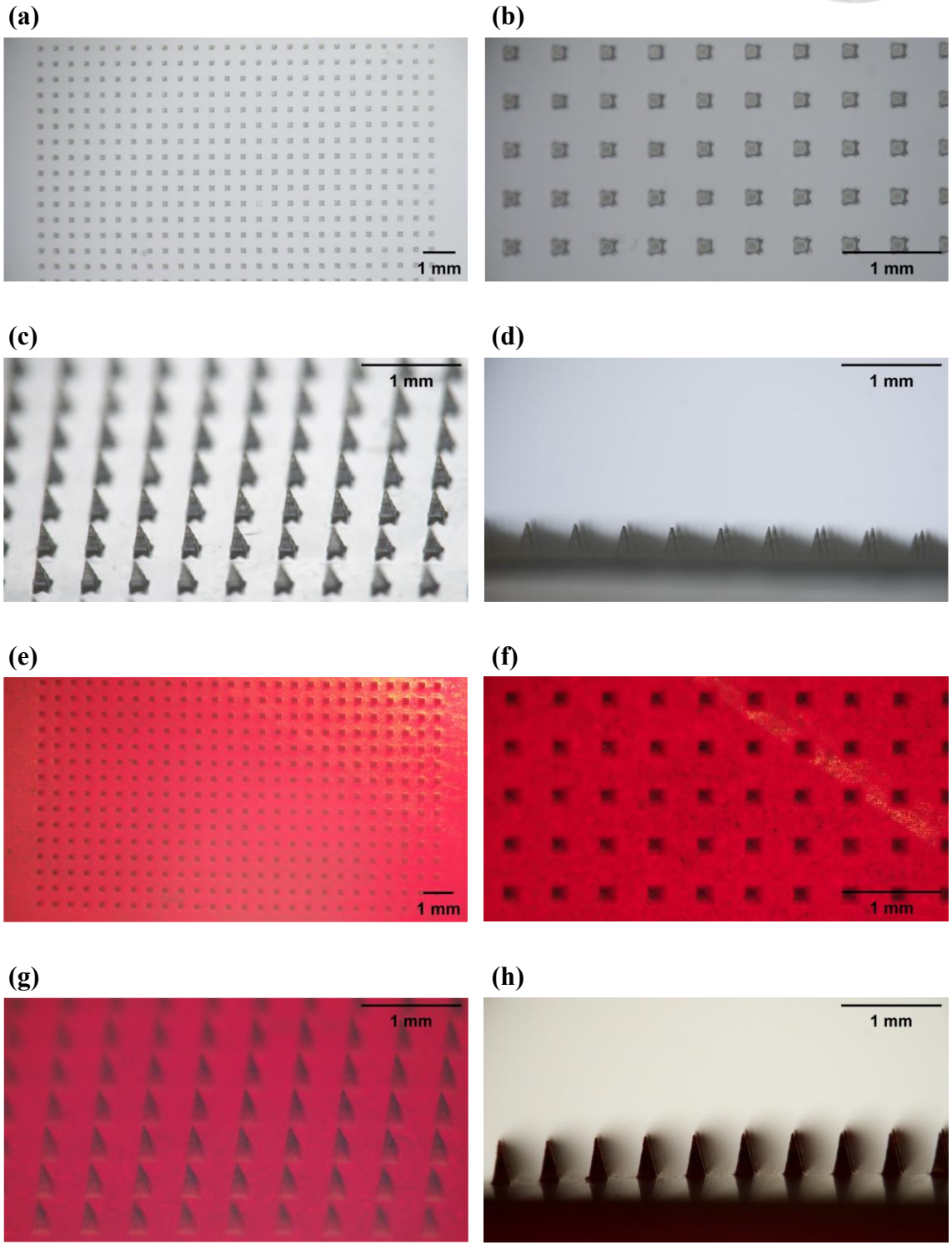

doi:10.6342/NTU202501655

Fig. 5.9. Optical microscope images of microneedle patches composed of 7 wt% PVA encapsulating 400 μg/mL MIL-100(Fe), with a needle length of 0.3 mm. Images (a-d) show the unstained microneedle patches captured at various framing angles and magnifications: (a) 0°, 10×; (b) 0°, 30×; (c) 45°, 30×; (d) 90°, 30×. Images (e-h) correspond to the same viewing parameters as (a-d), respectively, but show microneedle patches stained with rhodamine 6G.

5.4.2. Microneedle patches composed of 7 wt% PVA with a needle length of 1.5 mm

The 1.5 mm microneedles maintained good vertical alignment and a consistent pyramidal shape. Minor deformation at the needle base and tip was observed in certain areas, possibly caused by deformation during the demolding process. Despite this, the tips remained sufficiently sharp, and the majority of needles retained their structural integrity (**Fig. 5.10**).

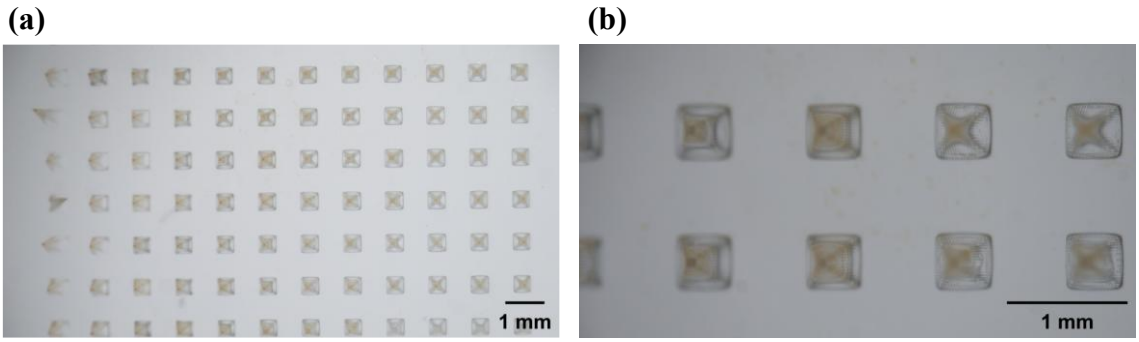

doi:10.6342/NTU202501655

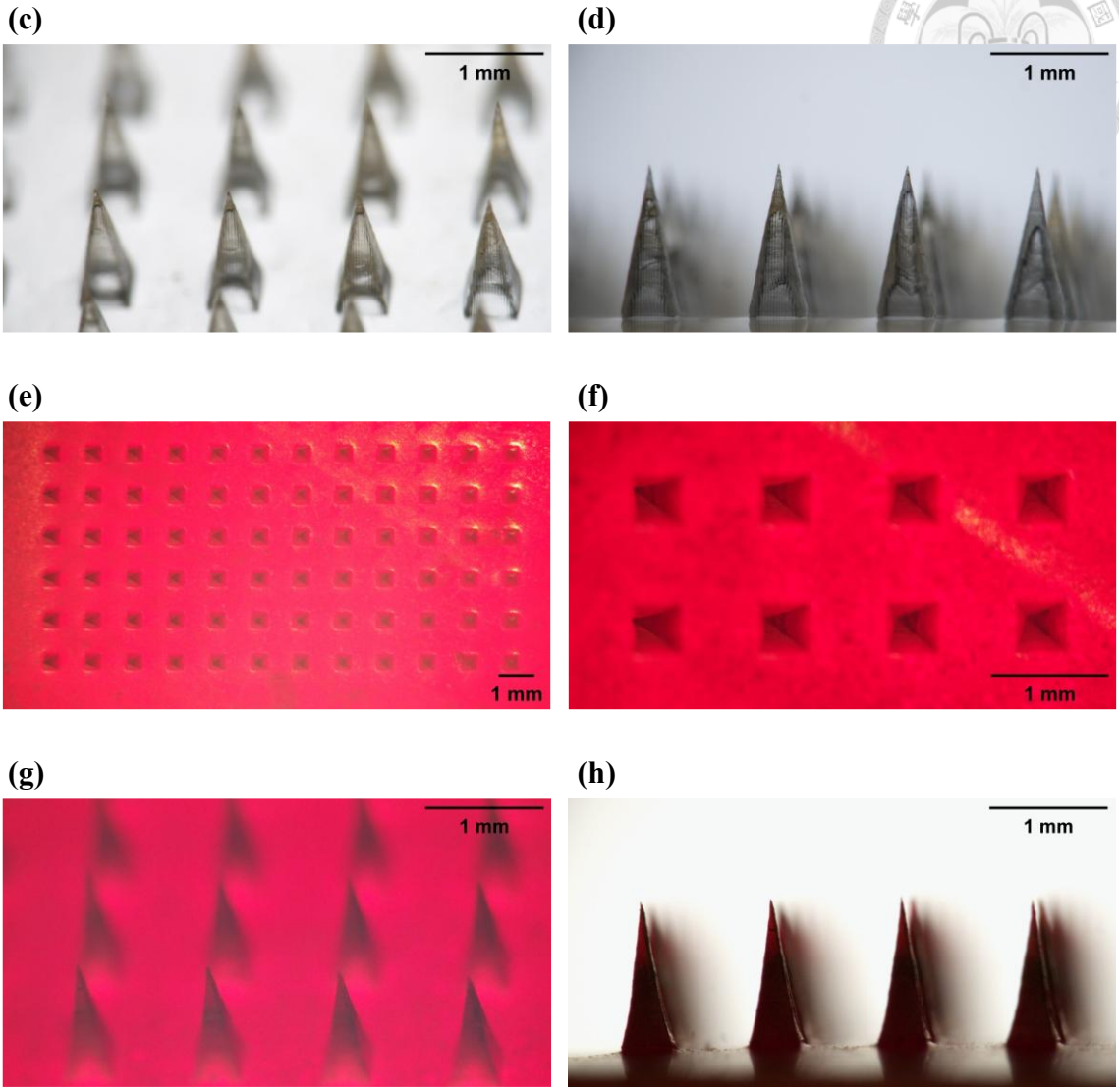

Fig. 5.10. Optical microscope images of microneedle patches composed of 7 wt% PVA encapsulating 400 μg/mL MIL-100(Fe), with a needle length of 1.5 mm. Images (a-d) show the unstained microneedle patches captured at various framing angles and magnifications: (a) 0°, 10×; (b) 0°, 30×; (c) 45°, 30×; (d) 90°, 30×. Images (e-h) correspond to the same viewing parameters as (a-d), respectively, but show microneedle patches stained with rhodamine 6G.

doi:10.6342/NTU202501655

5.4.3. Microneedle patches composed of 7 wt% PVA with a needle length of 2.0 mm

The 2.0 mm microneedles demonstrated uniform morphology, with all needles sharply tapered, vertically aligned, and free from structural defects such as collapse or fusion (**Fig. 5.11**).

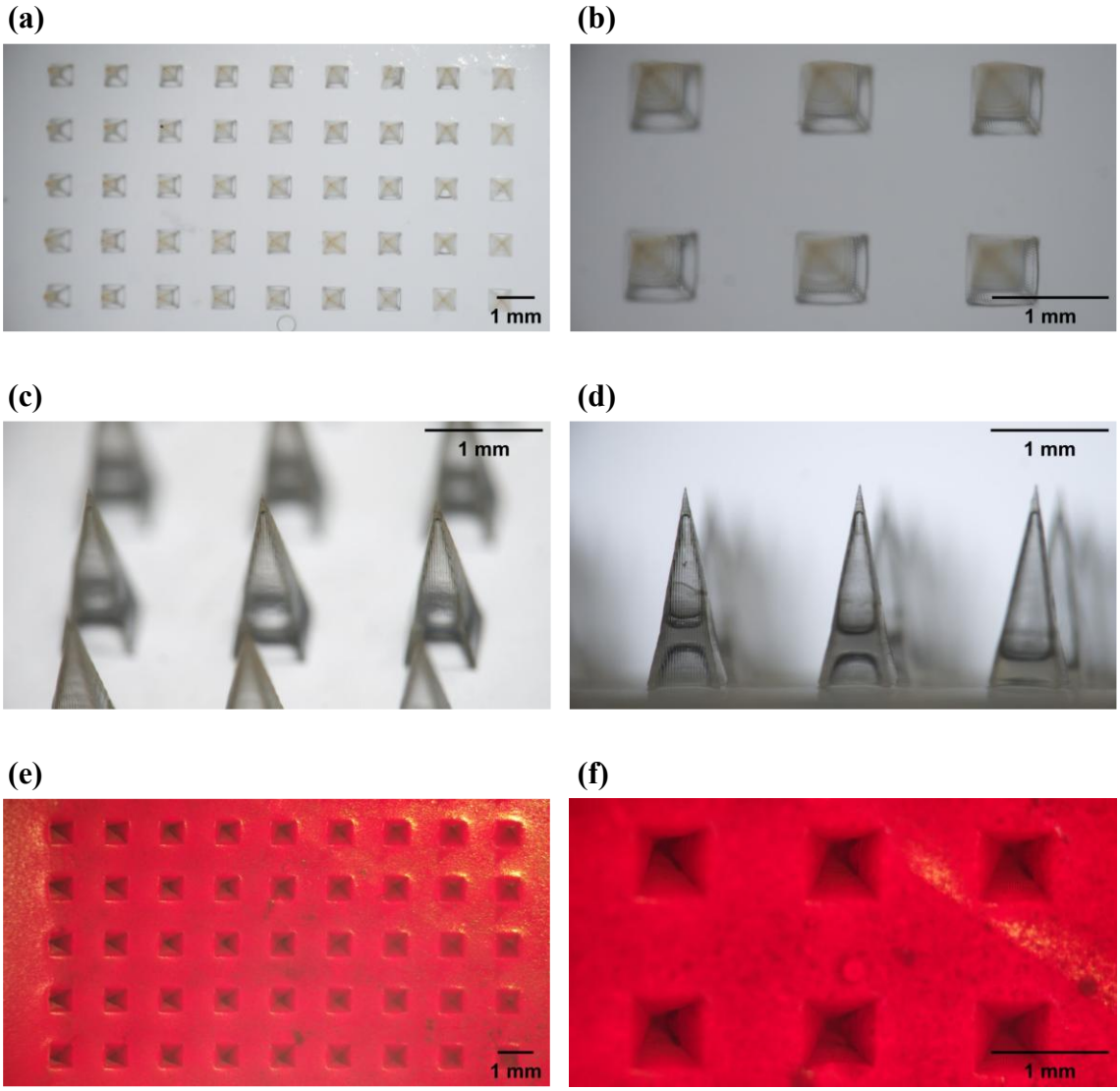

doi:10.6342/NTU202501655

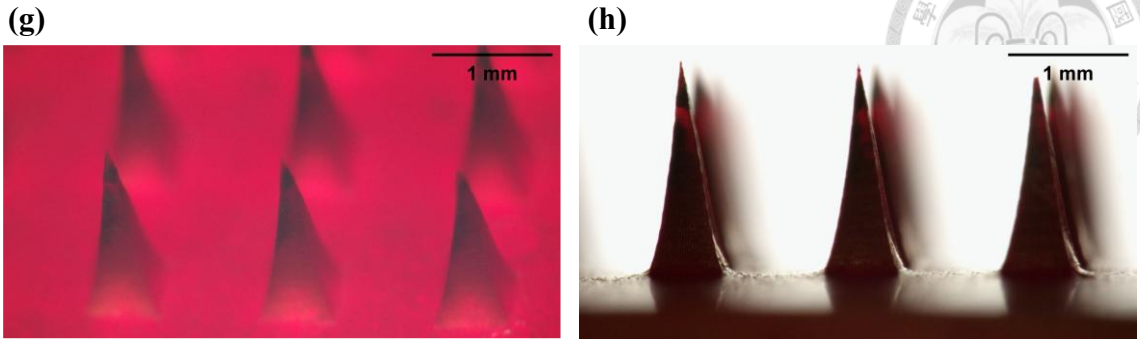

Fig. 5.11. Optical microscope images of microneedle patches composed of 7 wt% PVA encapsulating 400 μg/mL MIL-100(Fe), with a needle length of 0.3 mm. Images (a-d) show the unstained microneedle patches captured at various framing angles and magnifications: (a) 0°, 10×; (b) 0°, 30×; (c) 45°, 30×; (d) 90°, 30×. Images (e-h) correspond to the same viewing parameters as (a-d), respectively, but show microneedle patches stained with rhodamine 6G.

5.4.4. Microneedle patches composed of 7 wt% CMC with a needle length of 0.3 mm

The 0.3 mm CMC microneedles exhibited excellent shape accuracy and alignment. The images showed uniform arrays with clearly defined pyramidal tips (**Fig. 5.12**).

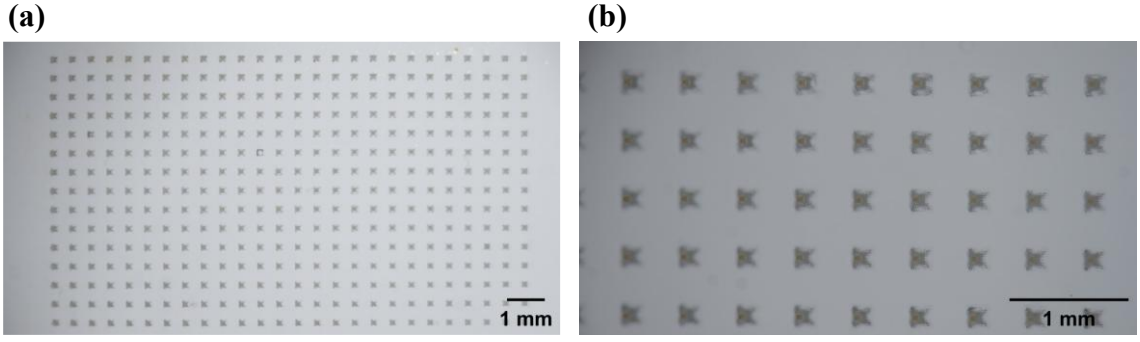

doi:10.6342/NTU202501655

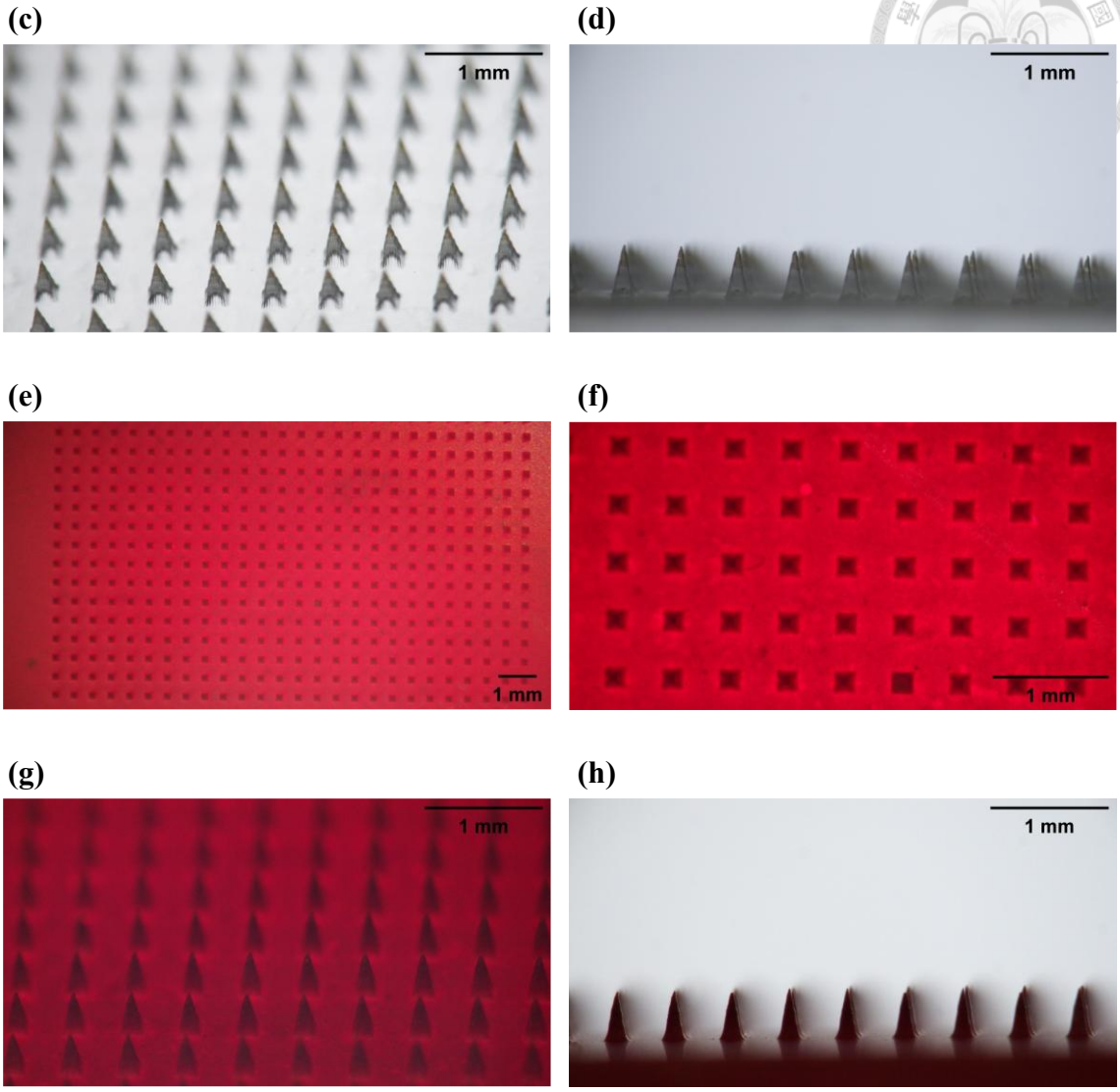

Fig. 5.12. Optical microscope images of microneedle patches composed of 7 wt% CMC encapsulating 400 μg/mL MIL-100(Fe), with a needle length of 0.3 mm. Images (a-d) show the unstained microneedle patches captured at various framing angles and magnifications: (a) 0°, 10×; (b) 0°, 30×; (c) 45°, 30×; (d) 90°, 30×. Images (e-h) correspond to the same viewing parameters as (a-d), respectively, but show microneedle patches stained with rhodamine 6G.

doi:10.6342/NTU202501655

5.4.5. Microneedle patches composed of 7 wt% CMC with a needle length of 1.5 mm

For the 1.5 mm CMC microneedles, the structures remained mostly consistent with well-defined shapes, although slight tip blunting was observed in some areas. This may be due to deformation that occurs during the demolding process. (**Fig. 5.13**).

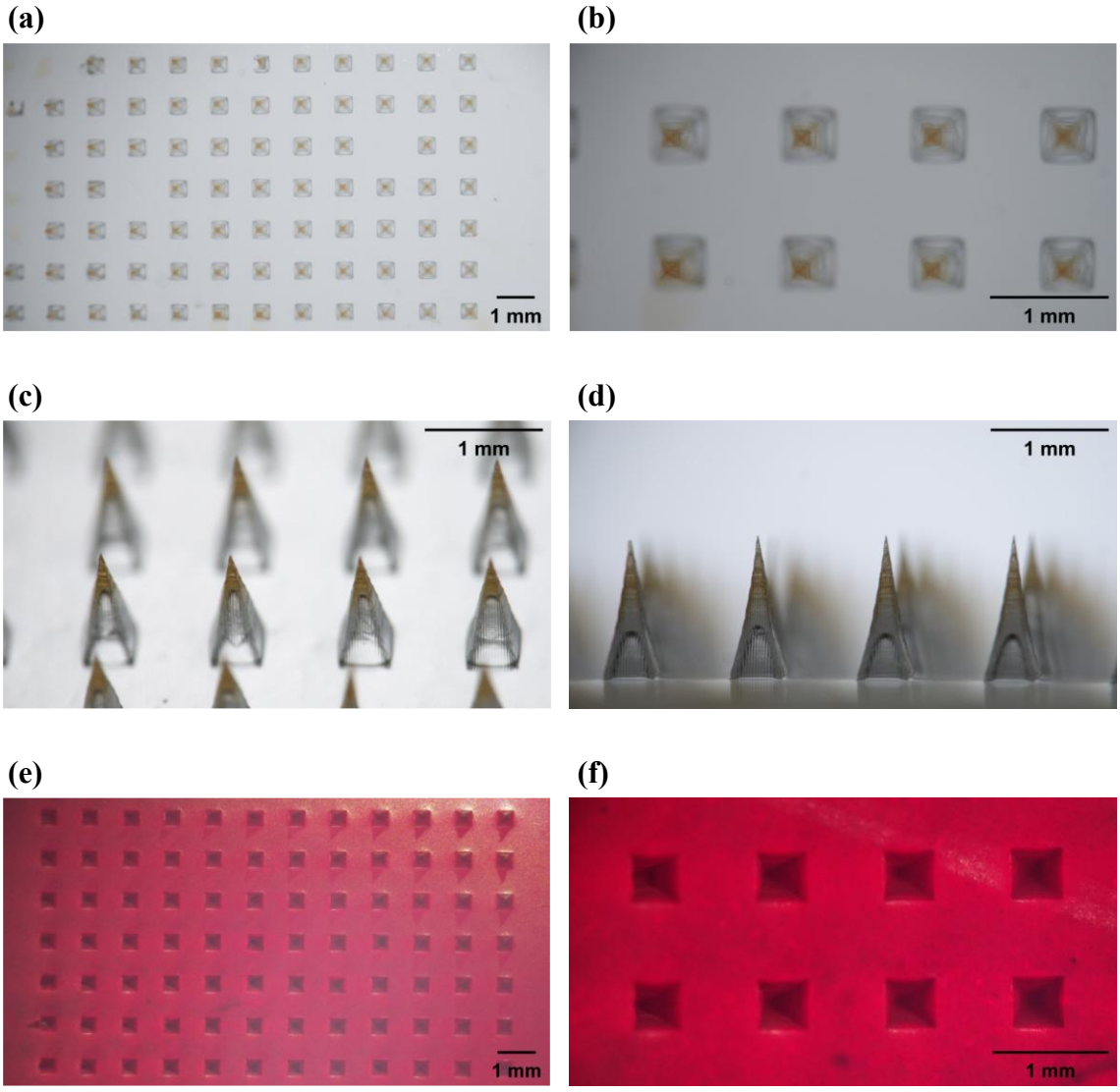

doi:10.6342/NTU202501655

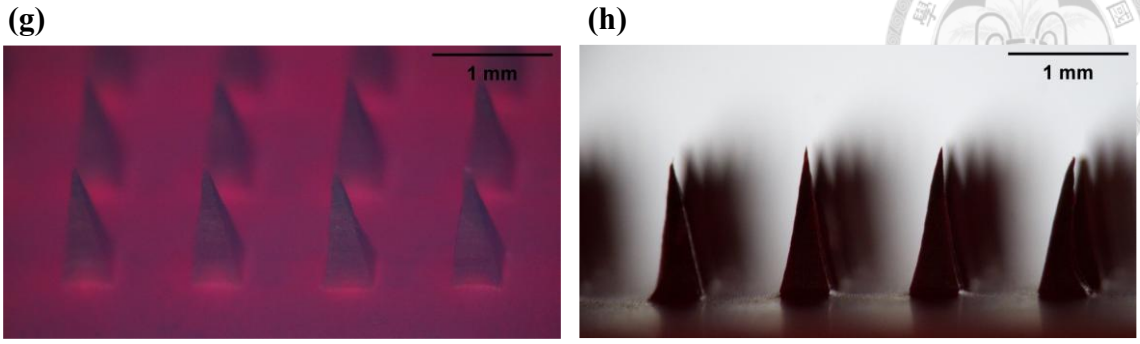

Fig. 5.13. Optical microscope images of microneedle patches composed of 7 wt% CMC encapsulating 400 μg/mL MIL-100(Fe), with a needle length of 1.5 mm. Images (a-d) show the unstained microneedle patches captured at various framing angles and magnifications: (a) 0°, 10×; (b) 0°, 30×; (c) 45°, 30×; (d) 90°, 30×. Images (e-h) correspond to the same viewing parameters as (a-d), respectively, but show microneedle patches stained with rhodamine 6G.

5.4.6. Microneedle patches composed of 7 wt% CMC with a needle length of 2.0 mm

The 2.0 mm CMC microneedles exhibited generally uniform morphology, with most needles displaying sharp tapering and vertical alignment. However, slight deformation at the base and tip was observed in some areas, possibly due to the rheological behavior of the polymer during the molding process (**Fig. 5.14**).

doi:10.6342/NTU202501655

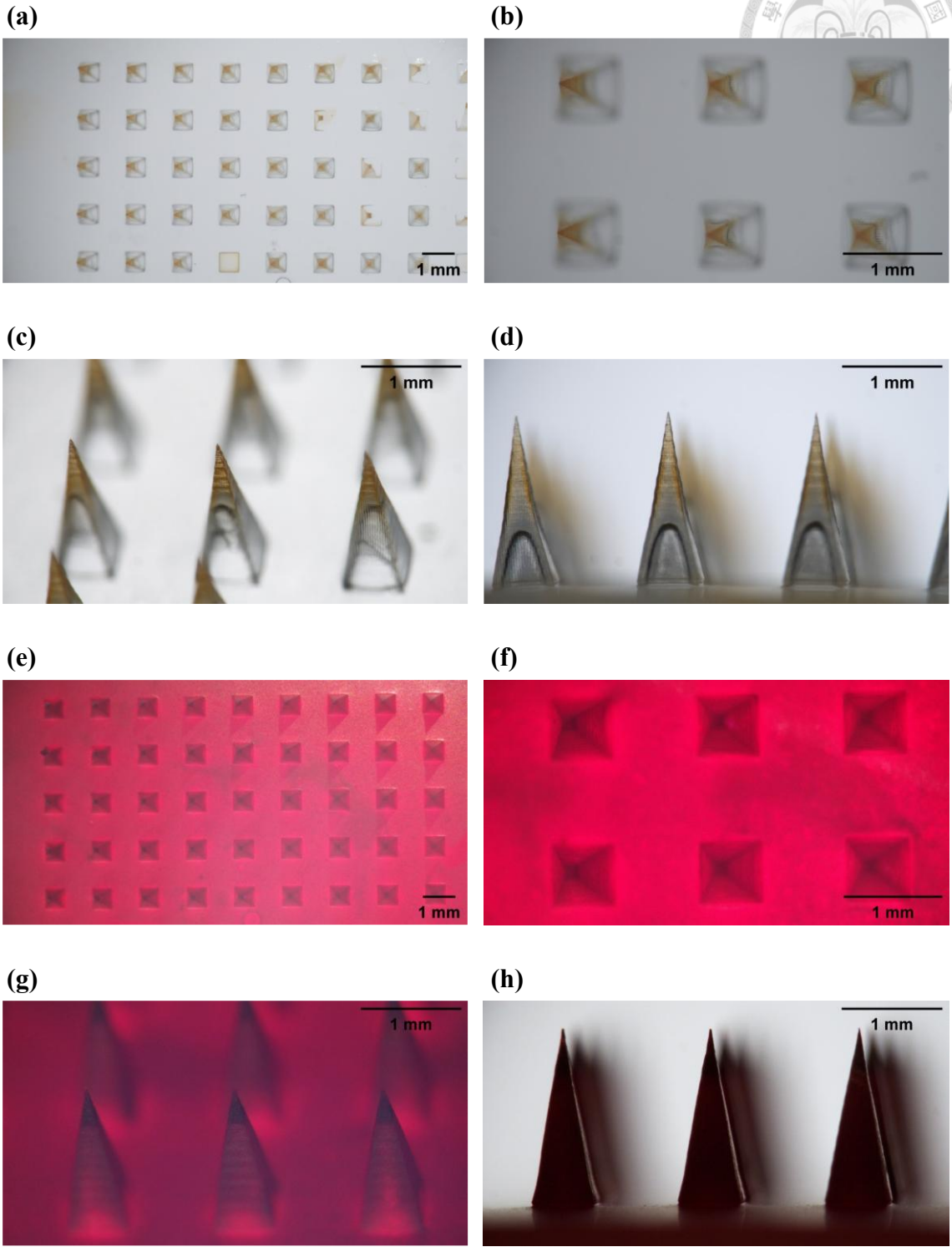

Fig. 5.14. Optical microscope images of microneedle patches composed of 7 wt% CMC encapsulating 400 μg/mL MIL-100(Fe), with a needle length of 2.0 mm. Images (a-d)

doi:10.6342/NTU202501655

show the unstained microneedle patches captured at various framing angles and magnifications: (a) 0°, 10×; (b) 0°, 30×; (c) 45°, 30×; (d) 90°, 30×. Images (e-h) correspond to the same viewing parameters as (a-d), respectively, but show microneedle patches stained with rhodamine 6G.

5.5. *In vitro* test for drug release depth in porcine skin

5.5.1. Insertion performance of 7 wt% PVA microneedles with varying lengths

As shown in **Fig. 5.15**, microneedle patches made of 7 wt% PVA with lengths of 0.3 mm, 1.5 mm, and 2.0 mm (arranged from left to right) were applied to porcine skin using a controlled insertion force of 12 N for 15 min using a DMA. Despite maintaining these consistent conditions, the images presented in **Figs. 5.16-5.18** reveal that none of the microneedles achieved full penetration through the skin layers. This incomplete insertion may not solely reflect the material properties of the 7 wt% PVA formulation, but rather the limited ability of the constant applied force to overcome the skin's mechanical resistance. Unlike manual application, which typically involves a brief and sharp force, the steady force provided by the DMA may have been insufficient to fully insert the microneedles into the tissue.

doi:10.6342/NTU202501655

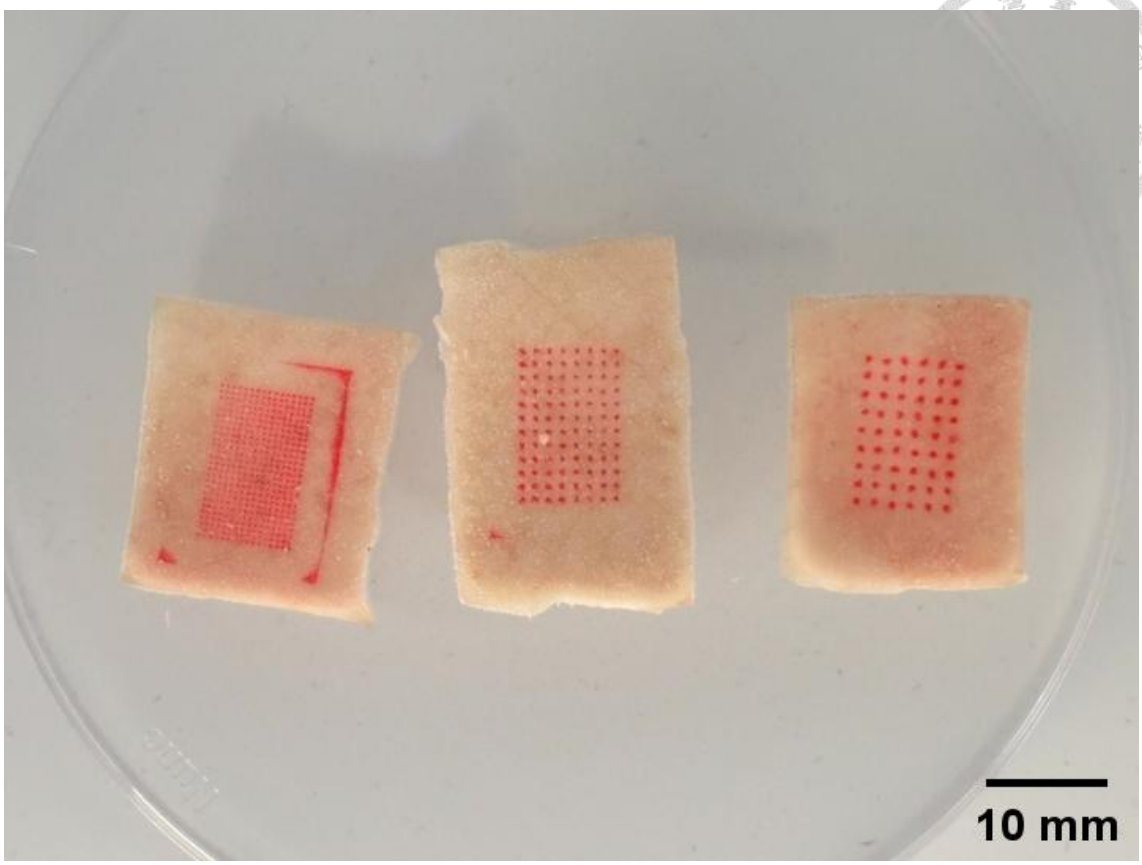

Fig. 5.15. Post-insertion images of porcine skin treated with 7 wt% PVA microneedles of different lengths (0.3 mm, 1.5 mm, and 2.0 mm from left to right).

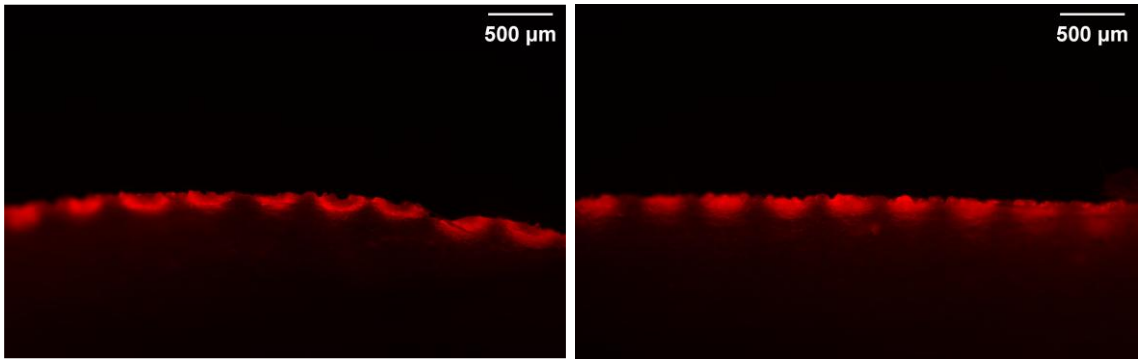

Fig. 5.16. Confocal microscope images of porcine skin treated with microneedle patches composed of 7 wt% PVA encapsulating 400 μg/mL MIL-100(Fe), with a needle length

doi:10.6342/NTU202501655

of 0.3 mm.

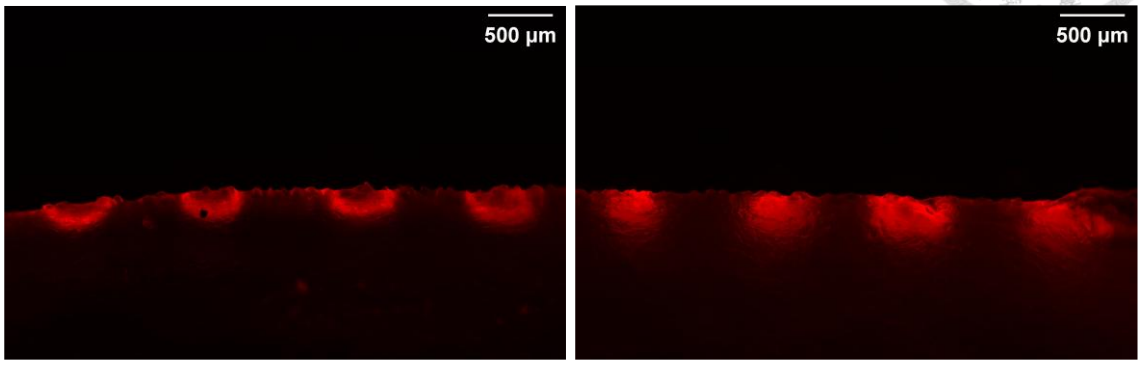

Fig. 5.17. Confocal microscope images of porcine skin treated with microneedle patches composed of 7 wt% PVA encapsulating 400 μg/mL MIL-100(Fe), with a needle length of 1.5 mm.

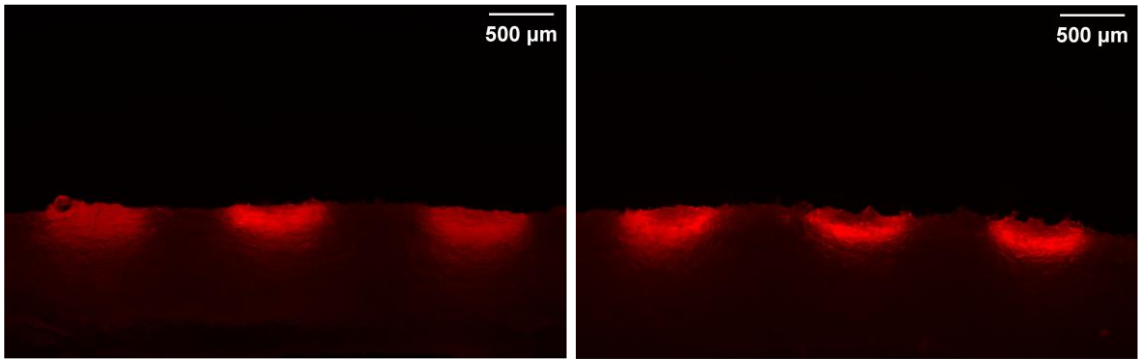

Fig. 5.18. Confocal microscope images of porcine skin treated with microneedle patches composed of 7 wt% PVA encapsulating 400 μg/mL MIL-100(Fe), with a needle length of 2.0 mm.

doi:10.6342/NTU202501655

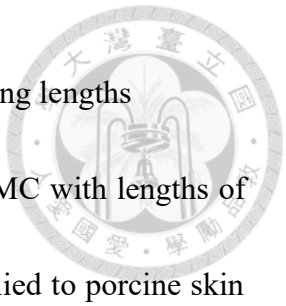

5.5.2. Insertion performance of 7 wt% CMC microneedles with varying lengths

As shown in **Fig. 5.19**, microneedle patches made of 7 wt% CMC with lengths of 0.3 mm, 1.5 mm, and 2.0 mm (arranged from left to right) were applied to porcine skin using a controlled insertion force of 12 N for 15 min using a DMA. Despite maintaining these consistent conditions, the images presented in **Figs. 5.20-5.22** reveal that none of the microneedles achieved full penetration through the skin layers. This outcome may be attributed not to the mechanical properties of the 7 wt% CMC formulation alone, but rather to the limited penetration capability of the constant applied force. Unlike real-world usage, where a brief, sharp force is typically applied by finger pressure, the steady loading from DMA may have been insufficient to overcome skin resistance. To validate this hypothesis, an additional test was conducted in which a rapid, manual force was applied to the microneedle patches. Furthermore, comparison of **Fig. 5.15** and **Fig. 5.19** reveals that the degradation rate of 7 wt% CMC microneedles is slower than that of 7 wt% PVA, which may further affect their ability to dissolve and anchor effectively upon insertion. These findings suggest that both the application method and the material properties must be considered when designing microneedle systems for reliable transdermal delivery.

doi:10.6342/NTU202501655

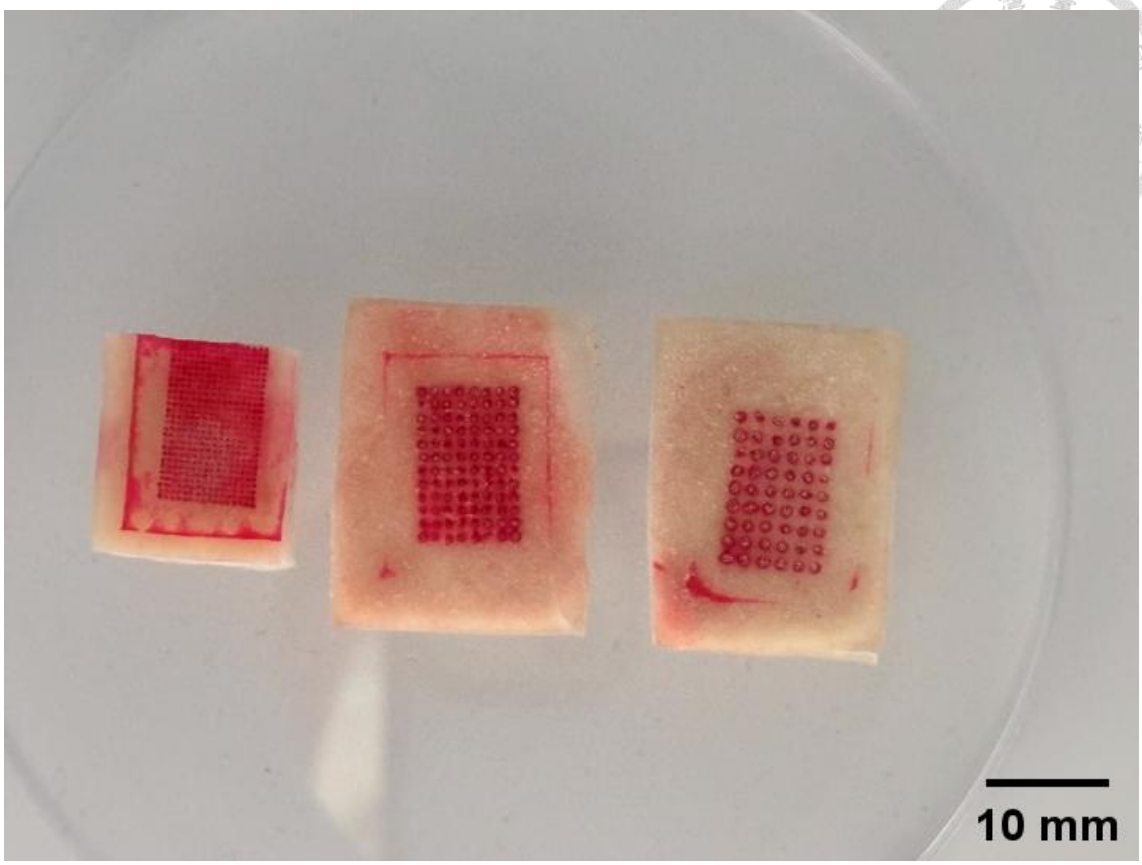

Fig. 5.19. Post-insertion images of porcine skin treated with 7 wt% CMC microneedles of different lengths (0.3 mm, 1.5 mm, and 2.0 mm from left to right).

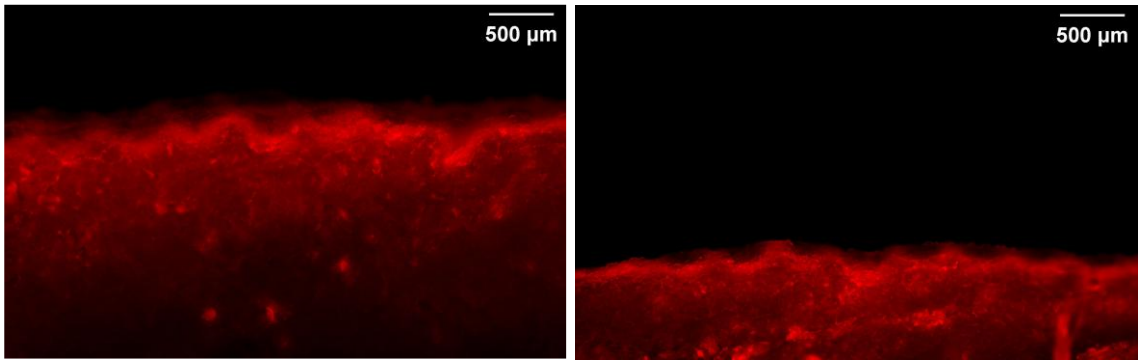

Fig. 5.20. Confocal microscope images of porcine skin treated with microneedle patches composed of 7 wt% CMC encapsulating 400 μg/mL MIL-100(Fe), with a needle length

doi:10.6342/NTU202501655

of 0.3 mm.

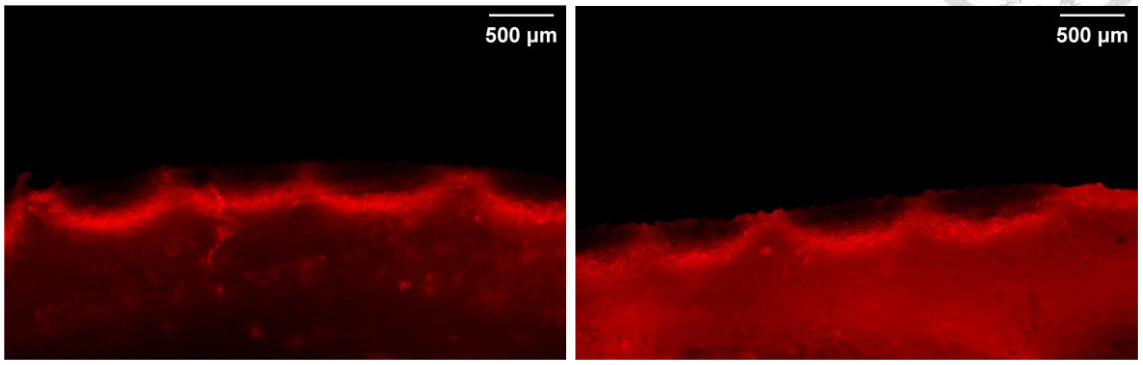

Fig. 5.21. Confocal microscope images of porcine skin treated with microneedle patches composed of 7 wt% CMC encapsulating 400 μg/mL MIL-100(Fe), with a needle length of 1.5 mm.

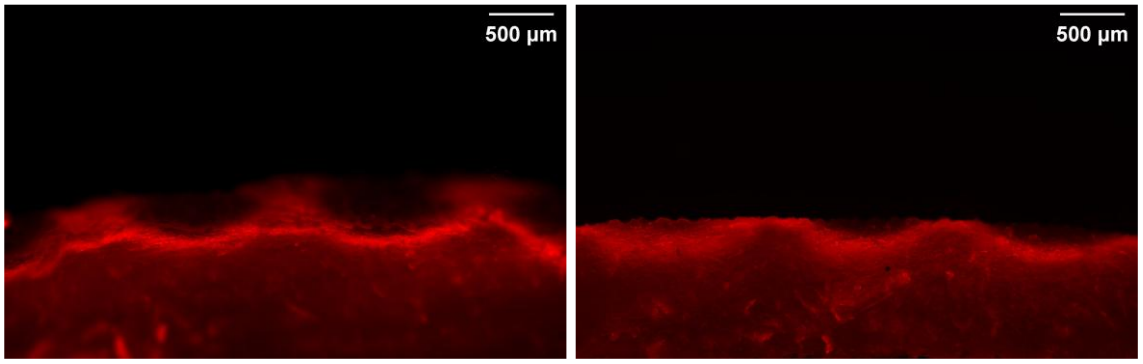

Fig. 5.22. Confocal microscope images of porcine skin treated with microneedle patches composed of 7 wt% CMC encapsulating 400 μg/mL MIL-100(Fe), with a needle length of 2.0 mm.

doi:10.6342/NTU202501655

5.5.3. Insertion performance of microneedle patches applied with manual pressure

As shown in **Fig. 5.23**, microneedle patches made of 7 wt% PVA, with lengths of 0.3 mm, 1.5 mm, and 2.0 mm, were applied to porcine skin using a sharp force from finger pressure to overcome the skin resistance. The resulting images indicate that some microneedles penetrated deeper into the skin layers compared to those inserted using a constant force via DMA. These findings partially suggest that a sudden application of force can enhance skin penetration. However, not all microneedles achieved full insertion, indicating that further investigation is needed into the structural design of the microneedles, as well as the properties and concentration of the polymer used in their fabrication.

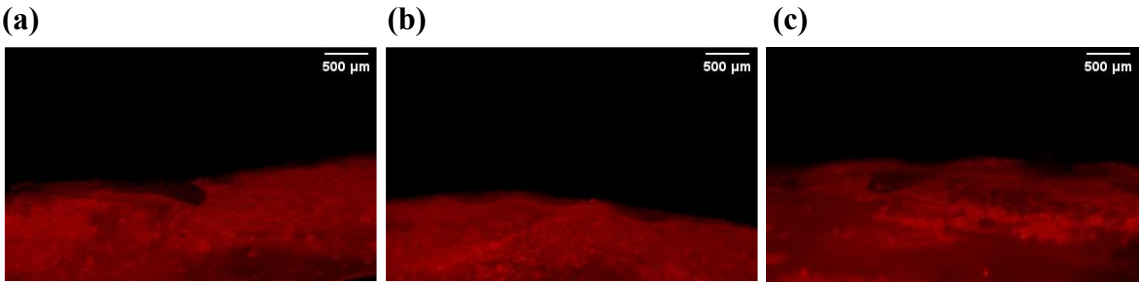

Fig. 5.23. Confocal microscope images of porcine skin treated with microneedle patches composed of 7 wt% PVA, encapsulating 400 μg/mL MIL-100(Fe), with a needle length of (a) 0.3 mm, (b) 1.5 mm, and (c) 2.0 mm. All patches were applied with manual pressure.

As shown in **Fig. 5.24**, microneedle patches made of 7 wt% CMC, with lengths of

doi:10.6342/NTU202501655

0.3 mm, 1.5 mm, and 2.0 mm, were applied to porcine skin using a sharp force exerted by finger pressure to overcome the skin resistance. Compared to the results presented in **Fig. 5.23**, a larger number of microneedles successfully penetrated the skin. This suggests that the CMC-based microneedles may have enhanced insertion capabilities under instantaneous force, potentially due to differences in material properties. These findings highlight the importance of polymer selection in optimizing microneedle performance for transdermal applications.

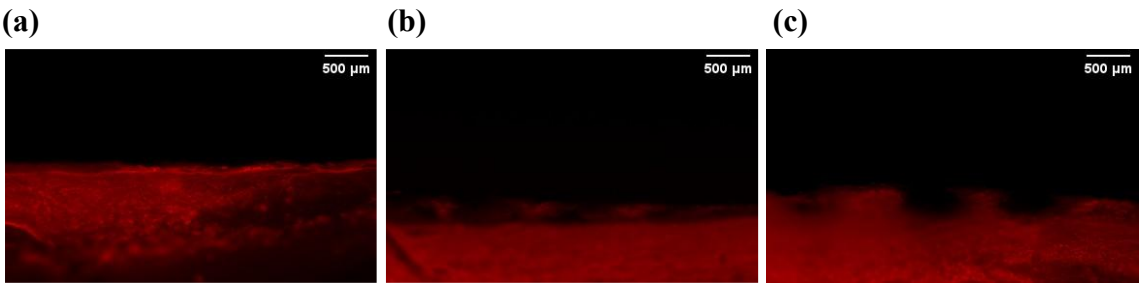

Fig. 5.24. Confocal microscope images of porcine skin treated with microneedle patches composed of 7 wt% CMC, encapsulating 400 μg/mL MIL-100(Fe), with a needle length of (a) 0.3 mm, (b) 1.5 mm, and (c) 2.0 mm. All patches were applied with manual pressure.

doi:10.6342/NTU202501655

6. Conclusion

In this study, a biocompatible and minimally invasive transdermal delivery system was developed by integrating iron-based metal-organic frameworks (i.e., MIL-100(Fe)) into dissolvable microneedle patches for the treatment of skin fibrosis. MIL-100(Fe) was successfully synthesized using a microwave-assisted hydrothermal method, resulting in particles with a microporous structure, moderate crystallinity, and a BET surface area of 949 m^2/g. Characterization by XRD, SEM, TEM, and DLS confirmed the structural integrity and uniformity of the synthesized MOF. Biocompatibility assessments showed that MIL-100(Fe) exhibited minimal cytotoxicity toward human keloid fibroblasts, maintaining over 90% cell viability across a wide range of concentrations. This highlights the material's suitability for biomedical applications, particularly in skin-related therapies.

Microneedle patches fabricated from 7 wt% polyvinyl alcohol (PVA) and 7 wt% sodium carboxymethyl cellulose (CMC) displayed a well-defined morphology. However, despite the clear geometry and alignment of the microneedle arrays, the patches did not achieve full penetration under either constant or manual application forces. This outcome suggests that the mechanical strength of the current formulations may be insufficient to overcome the barrier properties of the skin.

Therefore, further investigations are necessary to optimize the polymer

doi:10.6342/NTU202501655

concentration and refine the microneedle design. Adjustments in formulation stiffness, needle geometry, or fabrication techniques may enhance the efficiency of insertion and the depth of therapeutic delivery. These improvements will be crucial for advancing the clinical viability of this transdermal microneedle system in treating skin fibrosis.

doi:10.6342/NTU202501655

7. Future Work

Based on the promising results of this study, future work should focus on optimizing the mechanical strength and structural design of the microneedles. Since both the 7 wt% PVA and 7 wt% CMC microneedles demonstrated limited penetration under constant force and instantaneous force, adjusting polymer concentrations or modifying needle geometry could improve insertion efficiency.

Further *in vivo* studies are necessary to validate the therapeutic effect and biocompatibility of the MIL-100(Fe)-loaded microneedle system in skin fibrosis models. It will be critical to explore long-term safety, tissue response, and drug release behavior for clinical applications. Additionally, future research may investigate surface modifications or multifunctional designs to facilitate targeted delivery or imaging. With continued development, this system holds strong potential as a minimally invasive platform for the localized treatment of fibrotic skin conditions.

doi:10.6342/NTU202501655

References

[1] Diegelmann, R. F.; Evans, M. C., Wound healing: an overview of acute, fibrotic and delayed healing. *Front. biosci.* **2004**, *9*, 283-289.

[2] Nurden, A. T.; Nurden, P.; Sanchez, M.; Andia, I.; Anitua, E., Platelets and wound healing. *Front. Biosci.* **2008**, *13*, 3532-3548.

[3] Gonzalez, A. C. d. O.; Costa, T. F.; Andrade, Z. d. A.; Medrado, A. R. A. P., Wound healing-A literature review. *An. Bras. Dermatol.* **2016**, *91*, 614-620.

[4] Gabbiani, G., The myofibroblast in wound healing and fibrocontractive diseases. *J. Pathol.* **2003**, *200*, 500-503.

[5] Desmoulière, A.; Chaponnier, C.; Gabbiani, G., Tissue repair, contraction, and the myofibroblast. *Wound Repair Regen.* **2005**, *13*, 7-12.

[6] Chen, D.; Li, Q.; Zhang, H.; Kou, F.; Li, Q.; Lyu, C.; Wei, H., Traditional Chinese medicine for hypertrophic scars—A review of the therapeutic methods and potential effects. *Front. Pharmacol.* **2022**, *13*, 1025602.

[7] Shih, B.; Garside, E.; McGrouther, D. A.; Bayat, A., Molecular dissection of abnormal wound healing processes resulting in keloid disease. *Wound Repair Regen.* **2010**, *18*, 139-153.

[8] Wight, T. N.; Potter-Perigo, S., The extracellular matrix: an active or passive

doi:10.6342/NTU202501655

player in fibrosis? *Am. J. Physiol.-Gastr. L. Physiology* **2011**, *301*, G950-G955.

[9] Gauglitz, G. G.; Korting, H. C.; Pavicic, T.; Ruzicka, T.; Jeschke, M. G., Hypertrophic scarring and keloids: pathomechanisms and current and emerging treatment strategies. *Mol. Med.* **2011**, *17*, 113-125.

[10] Ehrlich, H. P.; Desmoulière, A.; Diegelmann, R. F.; Cohen, I. K.; Compton, C. C.; Garner, W. L.; Kapanci, Y.; Gabbiani, G., Morphological and immunochemical differences between keloid and hypertrophic scar. *Am. J. Pathol.* **1994**, *145*, 105.

[11] Penn, J. W.; Grobbelaar, A. O.; Rolfe, K. J., The role of the TGF-β family in wound healing, burns and scarring: a review. *Int. J. Burns Trauma* **2012**, *2*, 18.

[12] Ghazawi, F. M.; Zargham, R.; Gilardino, M. S.; Sasseville, D.; Jafarian, F., Insights into the pathophysiology of hypertrophic scars and keloids: how do they differ? *Adv. Skin Wound Care* **2018**, *31*, 582-595.

[13] Burd, A., So what is a keloid scar? *J. Plast. Reconstr. Aesthet. Surg.* **2008**, *61*, 1-3.

[14] Berman, B.; Maderal, A.; Raphael, B., Keloids and hypertrophic scars: pathophysiology, classification, and treatment. *Dermatol. Surg.* **2017**, *43*, S3-S18.

[15] Morelli Coppola, M.; Salzillo, R.; Segreto, F.; Persichetti, P., Triamcinolone acetonide intralesional injection for the treatment of keloid scars: patient selection

doi:10.6342/NTU202501655

and perspectives. *Clin. Cosmet. Investig. Dermatol.* **2018**, 387-396.

[16] Berman, B.; Bieley, H. C., Adjunct therapies to surgical management of keloids. *Dermatol. Surg.* **1996**, *22*, 126-130.

[17] Ogawa, R., The most current algorithms for the treatment and prevention of hypertrophic scars and keloids: a 2020 update of the algorithms published 10 years ago. *Plast. Reconstr. Surg.* **2022**, *149*, 79e-94e.

[18] Yang, J.; Yang, Y. W., Metal-organic frameworks for biomedical applications. *Small* **2020**, *16*, 1906846.

[19] Liu, X.; Liang, T.; Zhang, R.; Ding, Q.; Wu, S.; Li, C.; Lin, Y.; Ye, Y.; Zhong, Z.; Zhou, M., Iron-based metal-organic frameworks in drug delivery and biomedicine. *ACS Appl. Mater. Inter.* **2021**, *13*, 9643-9655.

[20] Quijia, C. R.; Lima, C.; Silva, C.; Alves, R. C.; Frem, R.; Chorilli, M., Application of MIL-100 (Fe) in drug delivery and biomedicine. *J. Drug Deliv. Sci. Tec.* **2021**, *61*, 102217.

[21] Bellido, E.; Guillevic, M.; Hidalgo, T.; Santander-Ortega, M. J.; Serre, C.; Horcajada, P., Understanding the colloidal stability of the mesoporous MIL-100 (Fe) nanoparticles in physiological media. *Langmuir* **2014**, *30*, 5911-5920.

[22] Duscher, D.; Neofytou, E.; Wong, V. W.; Maan, Z. N.; Rennert, R. C.; Inayathullah,

doi:10.6342/NTU202501655

M.; Januszyk, M.; Rodrigues, M.; Malkovskiy, A. V.; Whitmore, A. J., Transdermal deferoxamine prevents pressure-induced diabetic ulcers. *P. Natl. Acad. Sci.* **2015**, *112*, 94-99.

[23] Patel, A. V.; Shah, B. N., TRANSDERMAL DRUG DELIVERY SYSTEM: A REVIEW. *Pharma Sci. Monit.* **2018**, *9*.

[24] Jeong, W. Y.; Kwon, M.; Choi, H. E.; Kim, K. S., Recent advances in transdermal drug delivery systems: A review. *Biomater. Res.* **2021**, *25*, 1-15.

[25] Lee, I. C.; Lin, W. M.; Shu, J. C.; Tsai, S. W.; Chen, C. H.; Tsai, M. T., Formulation of two-layer dissolving polymeric microneedle patches for insulin transdermal delivery in diabetic mice. *J. Biomed. Mater. Res. A* **2017**, *105*, 84-93.

[26] Trommer, H.; Neubert, R., Overcoming the stratum corneum: the modulation of skin penetration: a review. *Skin Pharmacol. Phys.* **2006**, *19*, 106-121.

[27] McCrudden, M. T.; McAlister, E.; Courtenay, A. J.; González-Vázquez, P.; Raj Singh, T. R.; Donnelly, R. F., Microneedle applications in improving skin appearance. *Exp. Dermatol.* **2015**, *24*, 561-566.

[28] Tuan-Mahmood, T.-M.; McCrudden, M. T.; Torrisi, B. M.; McAlister, E.; Garland, M. J.; Singh, T. R. R.; Donnelly, R. F., Microneedles for intradermal and transdermal drug delivery. *Eur. J. Pharm. Sci.* **2013**, *50*, 623-637.

doi:10.6342/NTU202501655

[29] Golshirazi, A.; Mohammadzadeh, M.; Labbaf, S., The Synergistic Potential of Hydrogel Microneedles and Nanomaterials: Breaking Barriers in Transdermal Therapy. *Macromol. Biosci.* **2025**, *25*, 2400228.

[30] Park, J.-H.; Allen, M. G.; Prausnitz, M. R., Biodegradable polymer microneedles: fabrication, mechanics and transdermal drug delivery. *J. Control. Release* **2005**, *104*, 51-66.

[31] Singh, P.; Carrier, A.; Chen, Y.; Lin, S.; Wang, J.; Cui, S.; Zhang, X., Polymeric microneedles for controlled transdermal drug delivery. *J. Control. Release* **2019**, *315*, 97-113.

[32] Kandavilli, S.; Nair, V.; Panchagnula, R., Polymers in transdermal drug delivery systems. *Pharm. Technol.* **2002**, *26*, 62-81.

[33] Donnelly, R. F.; Singh, T. R. R.; Garland, M. J.; Migalska, K.; Majithiya, R.; McCrudden, C. M.; Kole, P. L.; Mahmood, T. M. T.; McCarthy, H. O.; Woolfson, A. D., Hydrogel-forming microneedle arrays for enhanced transdermal drug delivery. *Adv. Funct. Mater.* **2012**, *22*, 4879-4890.

[34] Jain, N.; Singh, V. K.; Chauhan, S., A review on mechanical and water absorption properties of polyvinyl alcohol based composites/films. *J. Mech. Behav. Mater.* **2017**, *26*, 213-222.

doi:10.6342/NTU202501655

[35] Kumar, A.; Han, S. S., PVA-based hydrogels for tissue engineering: A review. *Int. J. Polym. Mater. Polym. Biomater.* **2017**, *66*, 159-182.

[36] Wu, Y.; Xiang, Y.; Fang, J.; Li, X.; Lin, Z.; Dai, G.; Yin, J.; Wei, P.; Zhang, D., The influence of the stiffness of GelMA substrate on the outgrowth of PC12 cells. *Biosci. Rep.* **2019**, *39*, BSR20181748.

[37] Ling, M.-H.; Chen, M.-C., Dissolving polymer microneedle patches for rapid and efficient transdermal delivery of insulin to diabetic rats. *Acta Biomater.* **2013**, *9*, 8952-8961.

[38] Dadfar, S. M. M.; Kavoosi, G., Mechanical and water binding properties of carboxymethyl cellulose/multiwalled carbon nanotube nanocomposites. *Polym. Composite.* **2015**, *36*, 145-152.

[39] Chen, M.-C.; Huang, S.-F.; Lai, K.-Y.; Ling, M.-H., Fully embeddable chitosan microneedles as a sustained release depot for intradermal vaccination. *Biomaterials* **2013**, *34*, 3077-3086.

[40] Wang, L.; Chen, Q.; Yarlagadda, P. K.; Zhu, F.; Li, Q.; Li, Z., Single-parameter mechanical design of a 3D-printed octet truss topological scaffold to match natural cancellous bones. *Mater. Design* **2021**, *209*, 109986.

[41] Wang, M.; Hu, L.; Xu, C., Recent advances in the design of polymeric

doi:10.6342/NTU202501655

microneedles for transdermal drug delivery and biosensing. *Lab Chip* **2017**, *17*, 1373-1387.

[42] Peng, X.; Huang, J.; Qin, L.; Xiong, C.; Fang, J., A method to determine Young's modulus of soft gels for cell adhesion. *Acta Mech. Sinica* **2009**, *25*, 565-570.

[43] Taberlet, N.; Ferrand, J.; Camus, É.; Lachaud, L.; Plihon, N., How tall can gelatin towers be? An introduction to elasticity and buckling. *Am. J. Phys.* **2017**, *85*, 908-914.

[44] Pinto, V.; Ramos, T.; Alves, S.; Xavier, J.; Tavares, P.; Moreira, P.; Guedes, R. M., Comparative failure analysis of PLA, PLA/GNP and PLA/CNT-COOH biodegradable nanocomposites thin films. *Procedia Engineer.* **2015**, *114*, 635-642.

[45] Chen, W.; Wang, C.; Yan, L.; Huang, L.; Zhu, X.; Chen, B.; Sant, H. J.; Niu, X.; Zhu, G.; Yu, K., Improved polyvinylpyrrolidone microneedle arrays with non-stoichiometric cyclodextrin. *J. Mater. Chem. B* **2014**, *2*, 1699-1705.

[46] Zhang, F.; Shi, J.; Jin, Y.; Fu, Y.; Zhong, Y.; Zhu, W., Facile synthesis of MIL-100 (Fe) under HF-free conditions and its application in the acetalization of aldehydes with diols. *Chem. Eng. J.* **2015**, *259*, 183-190.

[47] Simon, M. A.; Anggraeni, E.; Soetaredjo, F. E.; Santoso, S. P.; Irawaty, W.; Thanh, T. C.; Hartono, S. B.; Yuliana, M.; Ismadji, S., Hydrothermal synthesize of HF-

doi:10.6342/NTU202501655

free MIL-100 (Fe) for isoniazid-drug delivery. *Sci. Rep.* **2019**, *9*, 16907.

[48] Le, B. T.; La, D. D.; Nguyen, P. T. H., Ultrasonic-assisted fabrication of MIL-100 (Fe) metal-organic frameworks as a carrier for the controlled delivery of the chloroquine drug. *ACS Omega* **2022**, *8*, 1262-1270.

[49] Gorban, I. E.; Soldatov, M. A.; Butova, V. V.; Medvedev, P. V.; Burachevskaya, O. A.; Belanova, A.; Zolotukhin, P.; Soldatov, A. V., L-Leucine loading and release in MIL-100 nanoparticles. *Int. J. Mol. Sci.* **2020**, *21*, 9758.

[50] Chen, G.; Leng, X.; Luo, J.; You, L.; Qu, C.; Dong, X.; Huang, H.; Yin, X.; Ni, J., In vitro toxicity study of a porous iron (III) metal-organic framework. *Molecules* **2019**, *24*, 1211.

doi:10.6342/NTU202501655